PERIOD TRIPLING IN A PARAMETRICALLY DRIVEN DUFFING-OSCILLATOR

FYNN JANSSEN

Bachelor's Thesis

Submitted to the Faculty of Mathmatics, Computer Science and Natural Sciences at RWTH-Aachen University

under the supervision of

Prof. Dr. Fabian Hassler

and

Prof. Dr. Markus Müller

JARA-Institute for Quantum Information

July 2022

Abstract

In this thesis, we study a Duffing-oscillator which is parametrically driven at thrice its resonance frequency. We investigate the period tripling with the focus on the inductance due to thermal fluctuations. To this end, we use the rotating-frame approximation as an ansatz, such that the investigation is reduced to the complex oscillation amplitude. Further, we determine the tunneling rate at which period tripling is induced analytically via the action such as numerically, to an exponential accuracy. We show that period tripling only occurs for a driving force that exceeds a certain threshold depending on the dissipation, the restoring force and the stabilizing force. In the regime of period tripling, we find that the tunneling rate is exponentially dependent on the negative inverse temperature, in the limit of small fluctuations.

CONTENTS

1

INTRODUCTION

This thesis investigates a parametric oscillator. In general, a parametric oscillator describes an oscillator with time-dependent parameters. If these parameters meet the right conditions, this can lead to an excitation of the system, which is called parametric excitation. [4]

An illustrative example of this behavior is the following. We consider a pendulum made of a massless string and a point mass at the end of this string. Further, the pendulum is attached to a motor which changes the length of the string periodically at twice the resonance frequency ω_0 and with the amplitude $|A| < 1$. This motion can be described by $L(t) = L_0[1 + A\sin(2\omega_0 t)]$, where $L_0 > 0$ is the average length of the string. Further, in the regime of small deflections of the pendulum, the system can be approximately described by a damped harmonic oscillator

$$\ddot{\phi} + \Gamma\dot{\phi} + \frac{g}{L(t)}\phi = 0. \tag{1.1}$$

If we investigate small changes in the length of the pendulum, *i. e.* $|A| \ll 1$, we can Taylor expand $1/L(t)$[1] and rewrite Eq. (1.1) as

$$\ddot{\phi} + \Gamma\dot{\phi} + \omega_0^2\phi = F\phi\sin(2\omega_0 t), \tag{1.2}$$

with the resonance frequency $\omega_0 = \sqrt{g/L_0}$ and the parameter which describes the driving force $F = A\omega_0^2$. In this form of the equation, we can explicitly see that the time-dependent pendulum length can be expressed as a parametrically driven oscillator, *i. e.* the driving force is time-dependent. In this example, the solution $\phi(t)$ oscillates at the resonance frequency ω_0.

Furthermore, due to the periodicity of the driving force the system has a symmetry. To understand this symmetry it is beneficial to consider the following example. We choose the initial conditions such that the pendulum has some constant velocity and zero amplitude. After a full period of the driving force the pendulum only fulfills half a period. Now, the pendulum is in the same position but moves in the opposite direction and the cycle repeats. Thus, there are two different

1 $(1+x)^{-1} \approx 1 - x$ for $x \ll 1$

solutions for the oscillation with a time shift of π/ω_0 which show the same behavior. This phenomenon is called period-doubling [1] since there are two different periods which describe the same motion.

This brief example provides the intuition of how parametric oscillators work and further introduces period multiplication, which can be traced back to a symmetry of the system. This thesis analyzes a parametrically driven Duffing-oscillator with a threefold symmetry which leads to period tripling.

Chapter overview

In Ch. 2 we qualitatively investigate the Duffing oscillator and the influence of the driving force, which oscillates with thrice of the resonance frequency. Based on the results, we propose the rotating-frame approximation as an ansatz, which leads to a differential equation of the oscillation amplitude. The resulting differential equation is analyzed in Ch. 3, where we investigate the fixed points, their stability and finally, discuss the dynamical properties of the amplitude.

After discussing the system at zero temperature, we introduce thermal fluctuations in Ch. 4. There, we introduce a method to numerically solve stochastic differential equations and investigate tunneling events due to thermal fluctuations analytically as well as numerically.

In Ch. 5 we revisit the Duffing oscillator beyond the rotating-frame approximation by analyzing the Poincaré map of the phase space. Based on the results, we discuss the validity of the rotating-frame approximation.

2

DESCRIPTION OF THE SYSTEM

2.1 THE PARAMETRICALLY DRIVEN DUFFING-OSCILLATOR

In this chapter, we investigate a Duffing-oscillator which is parametrically driven at thrice its resonance frequency and can be described by the following differential equation.

$$\ddot{x} + \Gamma\dot{x} + \omega_0^2 x + F\sin(\Omega t)\, x^2 + Ax^3 = 0 \tag{2.1}$$

This equation contains five independent parameters. The first three terms describe a damped harmonic oscillator, with the damping $\Gamma \geq 0$ and the resonance frequency $\omega_0 > 0$. Due to the additional cubic stabilizing force, characterized by the parameter $A > 0$, this equation describes a Duffing-oscillator. The stabilizing force is necessary to dominate the driving force Fx^2, with $F > 0$, for large oscillation amplitudes. Without the stabilizing force, the system would be divergent. Further, this force is parametrically driven, so it is modulated by an oscillation with frequency $\Omega = 3(\omega_0 - \Delta)$. The parameter $\Delta \geq 0$ is called detuning. It describes either a real experimental setup in which it is not possible to drive at the exact resonance frequency, or it describes an intentional offset to the resonance frequency. In this investigation, Δ describes a small perturbation in the oscillation frequency of the driving force, such that $\Delta \ll \Omega$.

In order to develop an intuition for this system, it is beneficial to investigate the energy $E = \dot{x}^2/2 + \omega_0^2 x^2/2 + Ax^4/4$, constructed by the sum of kinetic and potential energy. By multiplying $\dot{x}$ to Eq. (2.1) we find the total time derivative of the energy, which we substitute and therefore, obtain

$$\dot{E} = -\Gamma\dot{x}^2 - F\sin(\Omega t)\,\dot{x}x^2 = -2\Gamma \cdot E_{kin} - F\sin(\Omega t)\,\dot{x}x^2. \tag{2.2}$$

In general, if the energy of a system is conserved, it does not change over time. Therefore, the energy of this Duffing-oscillator is not conserved, since Eq. (2.2) is not necessarily zero. Furthermore, the first term is always negative and, therefore, describes an energy loss due to dissipation. However, the second term describes the energy change due to the driving force, which can be either positive or negative,

depending on the phase shift between the driving force and the oscillation $x(t)$.

2.1.1 *Numerical Solutions and Frequency Spectra*

For the further investigation, we numerically examine the system based on the solution of Eq. (2.1) for two different initial conditions and the corresponding frequency spectra. This makes it possible to better understand the behavior of the system.

At first, we discuss what kind of behavior we expect to find. Since the driving force depends on the amplitude squared we expect that we find different behaviors for different initial conditions. For initial conditions that are very close to the center in a $x, \dot{x}$-plane, we can neglect all terms of order $\mathcal{O}(x^2)$, resulting in a damped harmonic oscillator. Thus, we expect that in this limit the solution oscillates with the resonance frequency ω_0 and has an amplitude modulated by the exponential term $e^{-\Gamma t/2}$ due to the dissipation. Physically, in this scenario, the driving force has a very small influence compared to the restoring force and the dissipation, resulting in a vanishing oscillation amplitude. However, this implies that there can be a certain region in the phase space in which the driving force overcomes the restoring force. In this case, the strength of the restoring force has an important role.

Let us consider the following gedankenexperiment. If the parameter F, which describes the driving force, is negligibly small in comparison to the parameter A, which describes the stabilizing force, the driving force is always dominated. The stabilizing force determines the behavior in regions of large oscillation amplitudes and for decreasingly small oscillations the restoring force has the dominating role. However, if we now consider the case $F \gg A$, the stabilizing force only influences the system for very large oscillation amplitudes; it stabilizes the system. This implies that for intermediate amplitudes the driving force is stronger than both, the restoring force and the stabilizing force.

Thus, for a small stabilizing force and larger initial conditions, we expect to find oscillations with constant amplitude, such that the four forces—restoring, friction, stabilizing, and driving force—balance each other out, resulting in a state of equilibrium.

To analyze the behavior of the system, we investigate two solutions $x(t)$ and the belonging frequency spectra for different initial conditions. Furthermore, we make two simplifications. First, we investigate a more simple version of the system such that we neglect the detuning $\Delta = 0$

and afterwards we can generalize the findings. Hence, the driving force oscillates at exactly thrice the resonance frequency. Second, we analyze if we find a solution of the form

$$x(t) = a(t)\sin(\omega t), \tag{2.3}$$

where the solution has a time-depending amplitude $a(t)$ and primarily oscillates with some frequency ω. Therefore, we are looking for initial conditions such that $x(t)$ either vanishes or oscillates with a constant amplitude, in the limit of long times. In both scenarios, $a(t)$ converges to a constant value.

The results of the numerical calculations of the first case we discussed are presented in Figs. 2.1a and 2.1c. We can see that the oscillation amplitude is modulated by the factor $e^{-\Gamma t/2}$ and due to the peak at the resonance frequency ω_0 in the frequency spectrum[1], the spectrum has the typical form of a damped harmonic oscillator. Thus, these results match our expectations, and especially, the ansatz we

1 Figure 2.1a presents only one-tenth of $x(t)$ from which we calculated the frequency spectrum in order to obtain a greater resolution of the spectrum.

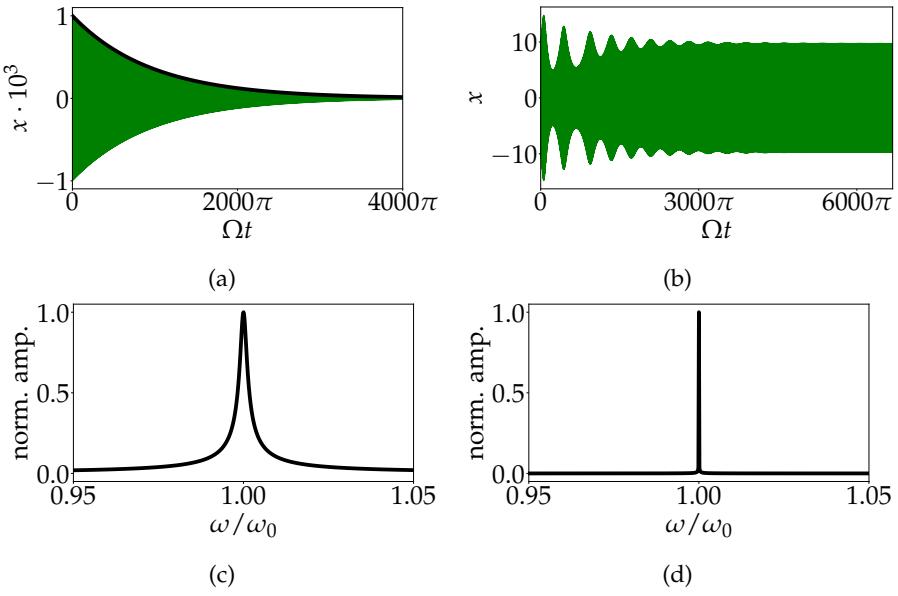

Figure 2.1: Numerically calculated solutions for $x(t)$ for the initial conditions $(10^{-3}, 0)$ (a) and $(10, 0)$ (b). Additionally, in Fig. (a) the amplitude is modulated by $e^{-\Gamma t/2}$ (black solid line). In Figs. (c) and (d) are the frequency spectra for these initial conditions, respectively. Note that the solutions $x(t)$ contain so many oscillations that the graphs appear like continuous areas. These plots are used to present the behavior of the amplitude which modulates the oscillations. To calculate the spectrum (c), the solution $x(t)$ is ten times as long as the one presented in Fig. (a), in order to increase the resolution. Analogously for Fig. (d), with the addition that only the region with constant amplitude was considered.

proposed can be used to describe the behavior of $x(t)$ in this regime.

The results of the second case, in which we investigate larger initial oscillation amplitudes, are presented in Figs. 2.1b and 2.1d. Here, we can see that the solution $x(t)$ converges to oscillations with a constant amplitude. Furthermore, the frequency spectrum was calculated for the solution $x(t)$ in the limit of the constant amplitude. This means that we considered the oscillations beyond approximately $\Omega t = 5000\pi$ in order to exclude the oscillations of the amplitude $a(t)$.

The spectrum has a primary peak at the resonance frequency ω_0 and additional peaks can be found at odd integer multiples of ω_0. These are not shown in Fig. 2.1d because the peak at $3\omega_0$ is more than two orders of magnitude smaller than the primary peak and further peaks are increasingly smaller. Furthermore, we can see that the amplitude $a(t)$ also oscillates and not just converges to the constant amplitude as in the previous case. However, the oscillation of the amplitude is significantly slower than the primary oscillation, which is necessary to separate these cases. Therefore, the ansatz applies in this case as well.

Thus, both cases are approximately in agreement with the expected form we proposed earlier and additionally, compatible with each other since both of them primarily oscillate with the same frequency—the resonance frequency ω_0. However, it has to be emphasized that this ansatz is not necessarily valid for arbitrary sets of parameters. This will be discussed in Ch. 5.

Furthermore, we want to intuitively understand the obtained results. To this end, we substitute the ansatz $x(t) = a(t)\sin(\omega_0 t)$ in Eq. (2.1). The first three terms of this equation describe a damped harmonic oscillator, as already discussed, which reproduces the oscillation at this frequency, *i.e.* if we insert the ansatz we only obtain oscillating terms with the same frequency. However, for the terms $\sin(\Omega t)x^2$ and x^3 we receive additional oscillation terms with higher frequencies. In the case of the term $\sin(\Omega t)x^2$, we can use trigonometric theorems and obtain three different terms. One of them oscillates with the resonance frequency ω_0 and the other two terms oscillate with $3\omega_0$ and $5\omega_0$. Analogously, x^3 leads to oscillations with the frequencies ω_0 and $3\omega_0$. Thus, the ansatz reproduces oscillation with frequency ω_0 with additional fast-oscillating terms that are odd integer multiples of ω_0.

Since the oscillations with the resonance frequency ω_0 appear more often than the fast-oscillating terms, the solution $x(t)$ mainly oscillates at this frequency. Furthermore, due to the appearance of these fast-oscillating terms, we can explain the small peaks in the frequency spectrum of the oscillations with a constant frequency. Hence, these

findings give an intuition for the frequency spectra.

To generalize this examination for $\Delta \neq 0$, we have to change one parameter, which leaves the arguments unchanged, if the limit $\Delta \ll \omega_0$ is investigated. Now, the ansatz $x(t)$ oscillates with the frequency $\Omega/3 = \omega_0 - \Delta$, such that the oscillation at this frequency is reproduced. In the case of large initial conditions, we argued that the terms oscillating with ω_0 would appear more often resulting in a dominant oscillation with this frequency. Now, this argument works in the same way since the driving force oscillates with $\Omega = 3(\omega_0 - \Delta)$.

However, in the limit of small initial conditions, we claimed that the differential equation can be approximated as a damped harmonic oscillator, which oscillates at its resonance frequency. This oscillation would be approximately independent of the driving force, so in this case, Δ has less influence than in the case of an oscillation with constant amplitude.

2.1.2 *Period Tripling*

At the end of this section, we interpret the results and their physical meaning. Therefore, we analyze the influence of the periodicity of the driving force.

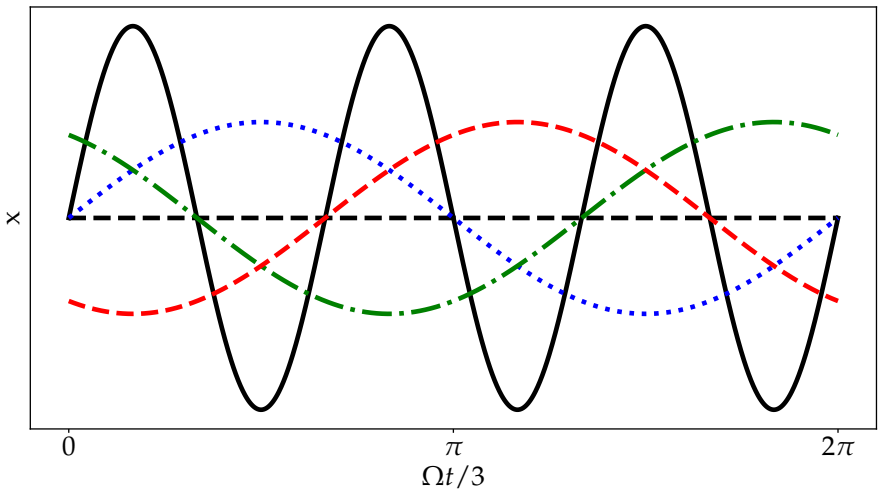

Figure 2.2: Demonstration of how the driving force (black) influences three different solutions (colored lines), each with a phase shift of $2\pi/3$, which oscillate at one-third the frequency of the driving force. The black dashed line represents the zero crossing and emphasizes the intersections between the driving force and the solutions. For clarity, the maximal amplitude of the driving force is twice as large as the amplitude of the solutions.

If we consider the transformation $t \to t + n \cdot 2\pi/\Omega$ of the differential equation (2.1), with $n \in \mathbb{Z}$, we find that the driving force does not change. For $n \in \{0, 1, 2\}$ we obtain the unchanged differential equation and two different transformations. Every other possible value of n describes one of those three cases due to the periodicity in time of $6\pi/\Omega$ in the solution $x(t)$. Further, if we define the new function $y(t) := x(t + n \cdot 2\pi/\Omega)$, the form of Eq. (2.1) is left unchanged after the considered transformation. Therefore, the functions $x(t)$ and $y(t)$ must have a similar behavior.

In general, there are systems that have a n-fold symmetry, which leads to period multiplication based on the same concept. Here, the terms $x^2 \sin(3\omega_0 t)$ and x^3 have to be generalized to $x^{n-1} \sin(n\omega_0 t)$, which reproduces the oscillation of ω_0 due to trigonometric theorems, and x^n which ensures the stability, respectively. [1]

This behavior is visualized in Fig. 2.2. We can see that each of the three colored lines intersects the driving force (black) at $x = 0$. At these intersections, the slopes of the driving force and of the respective solution $x(t)$ have the same sign.[2] This holds true for all three colored functions. Physically speaking, each individual oscillation $x(t)$ experiences the same force. Thus, there are three solutions with a shift in time of $2\pi/\Omega$, which is called period tripling.

2.2 ROTATING-FRAME APPROXIMATION

After this initial motivation, we choose an ansatz to investigate Eq. (2.1) in more detail, which is based on the initial approach that we discussed in the previous section in Eq. (2.3). We use the rotating-frame approximation[1]

$$x(t) = \Re\left(\beta(t)e^{-i\frac{\Omega}{3}t}\right) = \frac{\beta(t)e^{-i\frac{\Omega}{3}t} + \overline{\beta}(t)e^{i\frac{\Omega}{3}t}}{2} \tag{2.4}$$

to further examine the amplitude of the oscillations, given by the complex variable β. The introduction of the complex amplitude leads to a convenient description of the system because the period tripling transfers to the complex phase ϕ, if we use the polar coordinate representation $\beta(t) = r(t)e^{i\phi(t)}$.

The rotating-frame approximation considers a system with a primary oscillation—$e^{-i\frac{\Omega}{3}t}$—modulated by an amplitude—$\beta(t)$—which changes slowly compared to the rotating frame. Therefore, the rate of change of β is restricted to ω_0, which implies $\dot{\beta}/\beta \ll \omega_0$ and $\ddot{\beta}/\beta \ll \omega_0^2$. Furthermore, we receive restrictions to the parameters. To obtain these, we summarize the findings of the previous section.

We investigated the limits of small and large oscillation amplitudes. In the first case, the oscillation amplitude is exponentially decreasing with $\Gamma t/2$, which implies $\Gamma \ll \omega_0$. Further, the system oscillates at the resonance frequency, which does not match the frequency of the

2 This is not necessarily true, it is used here to provide a clear overview.

rotating frame, due to the detuning Δ. This difference of the oscillation is transferred to the complex amplitude. Thus, the detuning is also small in comparison to the resonance frequency ω_0, *i. e.* $\Delta \ll \omega_0$. In the case of large initial conditions, we found that the amplitude of β is constant in the limit $t \to \infty$ while the system oscillates with the frequency $\Omega/3$ which matches the rotating frame. Hence, we do not find any restrictions for this case.

After substituting $x(t)$ in the differential equation, we neglect all terms we discussed above and additionally, all fast oscillating terms that oscillate at integer multiples of $\Omega/3$. This leads to a complex differential equation for the amplitude β.

$$\dot{\beta} + (\gamma + i\Delta)\,\beta - \epsilon\overline{\beta}^2 + i\alpha\beta^2\overline{\beta} = 0 \tag{2.5}$$

Here, we define the parameters $\gamma \equiv \frac{\Gamma}{2}$, $\epsilon \equiv \frac{F}{8\omega_0}$, and $\alpha \equiv \frac{3A}{8\omega_0}$. Thus, the number of free parameters is reduced to four, since ω_0 only appears in fractions. To differentiate between the parameters of the Duffing-oscillator and Eq. (2.5), we name ϵ the driving strength and α the stabilizing strength. These quantities describe respectively the driving force and the stabilizing force normalized by the resonance frequency ω_0 which is a characteristic of the restoring force.

This equation is analyzed in detail in Ch. 3

3

ROTATING-FRAME DYNAMICS

In this chapter, we investigate the differential equation

$$\dot{\beta} + (\gamma + i\Delta)\,\beta - \epsilon\overline{\beta}^2 + i\alpha\beta^2\overline{\beta} = 0 \tag{3.1}$$

which was derived in Ch. 2. First, we determine the fixed points and their stability based on a first-order perturbation series, and afterwards, the dynamic of the system is analyzed. The goal is to develop a better understanding of the overall behavior of the system, before including thermal noise, which is considered in Ch. 4.

3.1 FIXED POINTS

The first step in understanding the system in the rotating-frame is to calculate the fixed points and their stability. Since Eq. (3.1) is a first-order differential equation with a damping term, we expect $\beta(t)$ to converge to a fixed point in the limit of long times. In order to calculate the fixed points we set $\dot{\beta} = 0$ in Eq. (3.1) and obtain

$$(\gamma + i\Delta)\,\beta_0 - \epsilon\overline{\beta}_0^2 + i\alpha\beta_0^2\overline{\beta}_0 = 0. \tag{3.2}$$

Since we expect to find period tripling, it is convenient to choose the polar coordinate representation $\beta_0 = r \cdot e^{i\phi}$, with the restrictions $r \in \mathbb{R}^+$ and $\phi \in [0, 2\pi]$. The real and imaginary parts of Eq. (3.2) have to be zero independently, so we receive two equations

$$0 = r\left[\gamma - \epsilon r\cos(3\phi)\right] \tag{3.3}$$

$$0 = r\left[\Delta + \epsilon r\sin(3\phi) + \alpha r^2\right], \tag{3.4}$$

which can be solved for r and ϕ. First, we find the trivial solution $r = 0$ and two additional solutions for the amplitude[1]

$$r_\pm = \frac{\epsilon}{\alpha}\cdot\sqrt{\frac{1}{2} - \frac{\alpha\Delta}{\epsilon^2} \pm \sqrt{\left(\frac{1}{2} - \frac{\alpha\Delta}{\epsilon^2}\right)^2 - \left(\frac{\alpha}{\epsilon^2}\right)^2\cdot(\gamma^2+\Delta^2)}}. \tag{3.5}$$

1 Note that $-r_\pm$ also would have solved these equations but this result is neglected since $r \geq 0$.

Based on the solutions for $r_\pm$, we obtain a restriction for ϵ that depends on Δ, γ, and α. First, we rewrite the square roots as $[x \pm (x^2 - y)^{1/2}]^{1/2}$ and find that $x > 0$ as well as $x^2 \geq y$, in order to find a real solution for either plus or minus. This is equivalent to $\epsilon > (2\alpha\Delta)^{1/2}$ and $\epsilon \geq \{2\alpha[(\gamma^2 + \Delta^2)^{1/2} + \Delta]\}^{1/2}$. Since the term in the square brackets is always greater than Δ, the first restriction is implied, if the second one is satisfied. However, if this condition is not satisfied the only fixed point is $r = 0$, *i.e.* $\beta(t)$ always converges with $e^{-\gamma t}$ to zero. This is in agreement with the physical understanding; if the magnitude of the driving strength ϵ falls below a certain limit, it is dominated by the dissipation γ and stabilizing strength α, resulting in a vanishing oscillation amplitude of the system.

Thus, to obtain period tripling, the investigation focuses on the limit $\Delta = 0$ and $\epsilon^2 \gg \gamma\alpha$. In this case, we obtain the restriction $\epsilon \geq \sqrt{2\alpha\gamma}$, which is always satisfied. In terms of the parameters of the parametrically driven Duffing-oscillation, we find the restriction for the driving force $F \geq \sqrt{24\Gamma A\omega_0}$. Here, we explicitly see that the driving force F is restricted to the damping, the restoring, and the stabilizing force, in order to find oscillations with a constant amplitude.

Furthermore, in the limit $\epsilon^2 \gg \gamma\alpha$, the Taylor expansion of Eq. (3.5) up to the second non-vanishing order is given by

$$\begin{aligned} r_+ &= \frac{\epsilon}{\alpha}\left[1 - \frac{\gamma^2\alpha^2}{2\epsilon^4} + \mathcal{O}\left(\left(\frac{\gamma\alpha}{\epsilon^2}\right)^4\right)\right] \\ r_- &= \frac{\gamma}{\epsilon}\left[1 + \frac{\gamma^2\alpha^2}{2\epsilon^4} + \mathcal{O}\left(\left(\frac{\gamma\alpha}{\epsilon^2}\right)^4\right)\right]. \end{aligned} \tag{3.6}$$

The second step to obtain the fixed points is to calculate the complex phase ϕ. To this end, we use Eqs. (3.3) and (3.4) to receive the expression $\tan(3\phi_\pm) = -\alpha r_\pm^2/\gamma$. To account for all possible solutions, we have to recall that Eqs. (3.3) and (3.4) are invariant under the transformation $\phi \to \phi + 2\pi n/3$, with $n \in \mathbb{Z}$. Hence, we obtain the three different phases

$$\begin{aligned} \phi_\pm &= -\frac{\arctan\left(\frac{\alpha r_\pm^2}{\gamma}\right)}{3} + \frac{2\pi n}{3} \quad , \qquad n \in \{0,1,2\} \\ &\approx -\frac{\arctan\left[\left(\frac{\epsilon^2}{\gamma\alpha}\right)^{\pm 1}\right]}{3} + \frac{2\pi n}{3} \end{aligned} \tag{3.7}$$

In this result, the period tripling is explicitly visible, since we have three solutions for both fixed points, each with a phase shift of $2\pi/3$. Hence, the system is symmetric under a rotation of this phase.

At last, we can determine the results in the limits $\gamma\alpha/\epsilon^2 \to 0$ and $\epsilon \to \epsilon_{\min} \equiv \sqrt{2\gamma\alpha}$. The first limit describes the case of a vanishing damping γ and stabilizing strength α in comparison to the driving strength ϵ. Here, we obtain $\phi_+ \in \left\{\frac{\pi}{2}, \frac{7\pi}{6}, \frac{11\pi}{6}\right\}$ and $\phi_- \in \left\{0, \frac{2\pi}{3}, \frac{4\pi}{3}\right\}$, so the inner and outer fixed points are not aligned with each other. This changes for the second limit. Here, the radii and the complex phases are equal, we receive $r_\pm = \sqrt{2}\gamma/\epsilon = (\gamma/\alpha)^{1/2}$ and $\phi_\pm \in \left\{\frac{7\pi}{12}, \frac{5\pi}{4}, \frac{23\pi}{12}\right\}$. Thus, the driving strength approaches the minimum value to obtain any fixed points, besides $\beta = 0$. At this critical force, there are only 4 fixed points in total instead of 7.[2]

3.2 STABILITY

In order to determine the stability of the fixed points, we investigate the system for small perturbations. Therefore, we use a perturbation series ansatz of the form $\beta(t) = \beta_0 + \delta\beta_1(t)$, with the stationary solution β_0 and a dimensionless parameter $\delta \ll 1$.

This ansatz is substituted in Eq. (3.1). In the resulting equation, we analyze the behavior of $\beta_1(t)$. If the solution converges to zero in the limit of long times, independent of the initial condition, the investigated fixed point is stable. Also, if $\beta_1(t)$ oscillates around the origin of the complex plane and, additionally, is periodic, *i. e.* $\beta(t)$ describes a closed path around the fixed point, the fixed point is considered to be stable. However, if there is one unstable direction, *i. e.* $\beta_1(t)$ increases over time, the considered fixed point is unstable.

After defining the ansatz and the different kinds of stability, we start with the analysis of $\beta_1(t)$. If we substitute $\beta(t) = \beta_0 + \delta\beta_1(t)$ in Eq. (3.1), we obtain three different types of terms. First, we find the terms of Eq. (3.2), whose sum is by definition zero. Second, there are terms of the order $\mathcal{O}(\delta^2)$ that we neglect, because we are only interested in a first-order perturbation series, so the differential equation becomes linear. The remaining terms are those of interest; a linear complex differential equation for $\beta_1(t)$

$$\dot{\beta}_1 + C_1\beta_1 + C_2\overline{\beta}_1 = 0. \tag{3.8}$$

The constants are defined as $C_1 = \gamma + i\Delta + 2i\alpha|\beta_0|^2$ and $C_2 = -2\epsilon\overline{\beta_0} + i\alpha\beta_0^2$. Since this is a complex differential equation, it can be rewritten as two coupled differential equations for β_1 and $\overline{\beta}_1$

$$\dot{\vec{x}} + \underline{\underline{M}} \cdot \vec{x} = 0, \tag{3.9}$$

$$\vec{x} = \begin{bmatrix} \beta_1 \\ \overline{\beta}_1 \end{bmatrix}, \quad \underline{\underline{M}} = \begin{bmatrix} C_1 & C_2 \\ \overline{C}_2 & \overline{C}_1 \end{bmatrix}, \tag{3.10}$$

2 Note that 2π were added to all phases, calculated by Eq. (3.7), which results in a more clear and equivalent representation

with the general solution $\vec{x} = e^{-\underline{\underline{M}}t} \cdot \vec{x}_0$ and the initial condition $\vec{x}_0 = (\beta_{1,0}, \overline{\beta}_{1,0})^T$. The eigenvalues $\lambda_{1,2}$ of the matrix $\underline{\underline{M}}$ are crucial for the behavior of $\beta_1(t)$ and the real parts are decisive for the stability due to the matrix exponential. There are two possible scenarios that have to be distinguished:

- $\Re(\lambda_{1,2}) \geq 0$: stable
- $\Re(\lambda) < 0$: unstable[3]

It has to be emphasized that a fixed point is considered to be unstable if it has one unstable direction. Therefore, if the real part of only one eigenvalue of $\underline{\underline{M}}$ is less than zero, the fixed point is considered to be unstable. The imaginary part of the eigenvalues leads to rotations in the complex plane and, thus, has no contribution to the stability. The calculation of the eigenvalues yields

$$\begin{aligned} \lambda_{1,2} &= \Re(C_1) \pm \sqrt{|C_2|^2 - \Im(C_1)^2} \\ &= \gamma \pm \sqrt{4\epsilon^2|\beta_0|^2 - 3\alpha^2|\beta_0|^4 + 4\alpha\epsilon\Im(\beta_0^3) - \Delta^2}. \end{aligned} \tag{3.11}$$

Here, the only term depending on the complex phase ϕ is $\Im(\beta_0^3)$. Therefore, the eigenvalues do not depend on the choice of $\phi_\pm$ due to the symmetry of $2\pi/3$ rotations, which is in agreement with the expectations. Now, we have to differentiate between the three cases $r = 0$ and $r_\pm$. The trivial case, $r = 0$, leads to $\lambda_{1,2} = \gamma \pm i\Delta$ and therefore, $\Re(\lambda_{1,2}) = \gamma \geq 0$. Thus, this fixed point is stable. The imaginary parts of these eigenvalues describe oscillations around the origin with the frequency Δ. This oscillation is in agreement with the argumentation of Sec. 2.1; in the limit of small initial conditions, the system can be approximated as a damped harmonic oscillator, which oscillates at its resonance frequency ω_0. Since we choose the rotating-frame approximation which oscillates at the frequency $\Omega/3 = \omega_0 - \Delta$, the oscillations with frequency Δ are transferred to the complex amplitude β.

Interestingly, for $\gamma < 0$ the fixed point $\beta = 0$ would be unstable. This is in agreement with the physical understanding, since $\gamma < 0$ would imply that the system gains energy through friction, thus, the oscillation amplitude β would never vanish.

For the fixed points $r_\pm$, we analyze the case of $\Delta = 0$, since the detuning describes a small perturbation of the resonance frequency and is in this examination also small in comparison to the other parameters. Therefore, it has no decisive influence on the behavior of the system other than the rotation around the point $r = 0$.

For $r_\pm$, we can use the first order of the approximation in Eq. (3.6) and the limit of the complex phases $\phi_\pm$. In this limit, for the inner fixed points we obtain $\lambda_{1,2} = \gamma \pm \gamma\sqrt{4 - 3\gamma^2\alpha^2/\epsilon^4}$. Here, the second term in the square root can be neglected due to the considered limit. Thus, we approximately receive $\lambda_{1,2} = \gamma \pm \gamma\sqrt{4}$ such that one of the

3 Note that the appearance of no indices implies that the condition only needs to be satisfied for at least one eigenvalue.

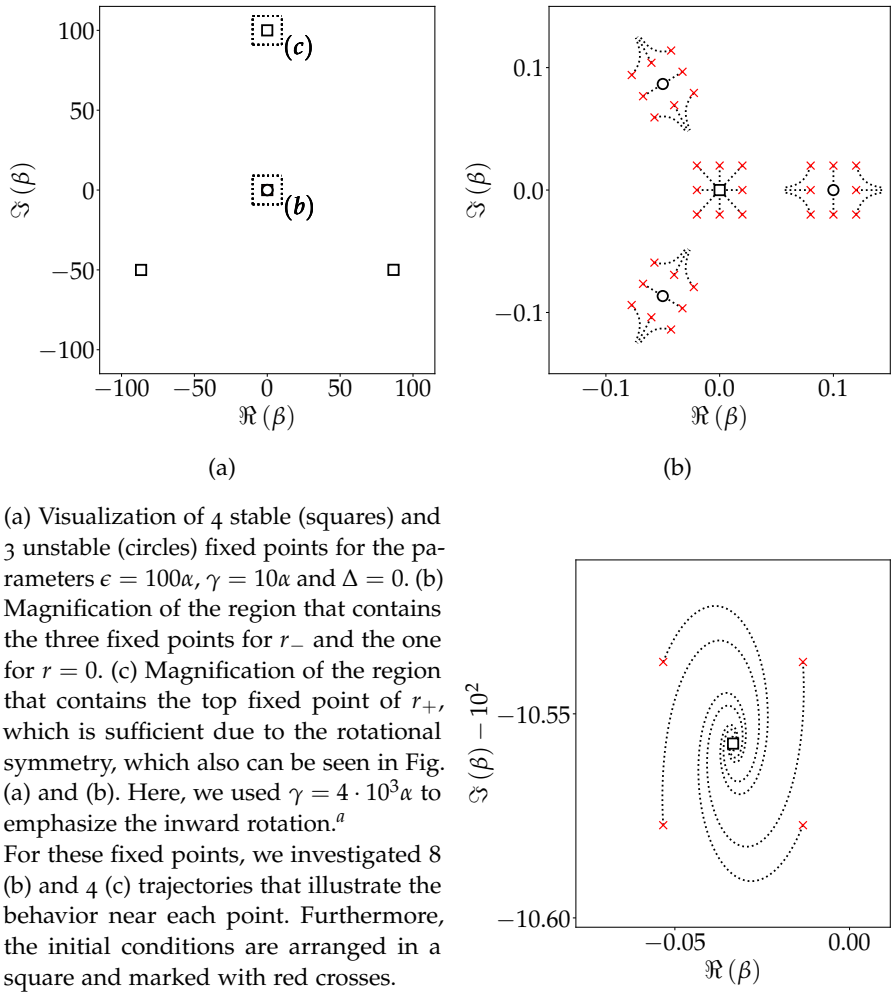

(a) (b)

(c)

(a) Visualization of 4 stable (squares) and 3 unstable (circles) fixed points for the parameters $\epsilon = 100\alpha$, $\gamma = 10\alpha$ and $\Delta = 0$. (b) Magnification of the region that contains the three fixed points for r_- and the one for $r = 0$. (c) Magnification of the region that contains the top fixed point of r_+, which is sufficient due to the rotational symmetry, which also can be seen in Fig. (a) and (b). Here, we used $\gamma = 4 \cdot 10^3\alpha$ to emphasize the inward rotation.[a]
For these fixed points, we investigated 8 (b) and 4 (c) trajectories that illustrate the behavior near each point. Furthermore, the initial conditions are arranged in a square and marked with red crosses.

a Note that these values for ϵ and γ would violate the constraint $\epsilon^2 \geq \gamma\alpha$, but in this case, it does not lead to problems since the differential equation was linearized.

Figure 3.1

eigenvalues is less than zero. Therefore, the inner fixed points are unstable.

The outer fixed points lead to $\lambda_{1,2} = \gamma \pm i\sqrt{3}\epsilon^2/\alpha$, such that $\Re(\lambda_{1,2}) > 0$. Therefore, the outer fixed points are stable. The imaginary part describes an oscillation with frequency $\omega = \sqrt{3}\epsilon^2/\alpha$. Further, in the case of $\gamma = 0$ these fixed points are still stable, but perturbations only lead to closed paths around the fixed points. These properties of the outer fixed points are discussed in the next section.

Next to the different types of fixed points r_+ and r_-, we discuss the limit $\epsilon \to \epsilon_{\min}$, such that these fixed points converge to the same

values, resulting in 3 fixed points instead of 6.[4] In this case, we obtain the eigenvalues $\lambda_{1,2} = \gamma \pm \gamma$. Thus, in this limit, the fixed points have one stable and one undefined direction. The eigenvalue $\lambda = 0$ describes a saddle-point which cannot be analyzed with a linearized differential equation. However, due to the stabilizing strength which does not allow diverging oscillation amplitudes, the unstable direction of the saddle-point results in a trajectory leading to the center.

In order to check the results, we analyze the solution for $\beta_1(t)$ numerically. To this end, $\beta(t) = \beta_0 + \delta\beta_1(t)$ is presented in the complex plane, with $\Re(\beta)$ as the x- and $\Im(\beta)$ as the y-axis. This representation is similar to the phase space outside the rotating frame, which we discuss in detail in Ch. 5. However, to analyze the behavior of $\beta_1(t)$ we create a small grid of initial conditions in the complex plane and calculate the approximated solution $\beta(t)$ for each initial condition. The resulting plots are shown in Fig. 3.1. It is visible that $r = 0$ and the outer fixed points are stable, while the fixed points for r_- are unstable. Furthermore, we can see the expected rotation around r_+ and that r_- is a saddle-point, *i. e.* it has both stable and unstable directions. Hence, the analytical results and numerical data are in agreement.

3.3 DYNAMICS OF THE SYSTEM

Now, we want to study the dynamical properties of the system. First, we discuss the stability maps with an included streamline plot for a given set of parameters and two different values of ϵ, which is presented in Fig. 3.2. The stability map is constructed of a grid of initial conditions and each point in that grid has an assigned color. This color indicates to which stable fixed point the solution $\beta(t)$ converges for the corresponding initial condition. The streamline plot (light blue) represents multiple short trajectories of the solution $\beta(t)$ for different initial conditions. The trajectories contain arrows that indicate the direction of the movement.

We can see that there are trajectories that oscillate multiple times around all three outer fixed points until they converge to one of the fixed points r_+ or $r = 0$. Additionally, all three colors are separated by a small black region, so the trajectories which converge into the center show similar behavior. Here, the difference is that three different ways lead to this fixed point—$r = 0$. Further, the width of the colored regions decreases with increasing distances from the origin. Thus, in these regions, the system shows chaotic behavior. For increasing values of ϵ, this behavior emerges more rapidly (see Fig. 3.2b). At last, it has to be emphasized that the fixed point $r = 0$ and its stability are

4 Note that these numbers only refer to the fixed points $r_\pm$ and not the fixed point $r = 0$.

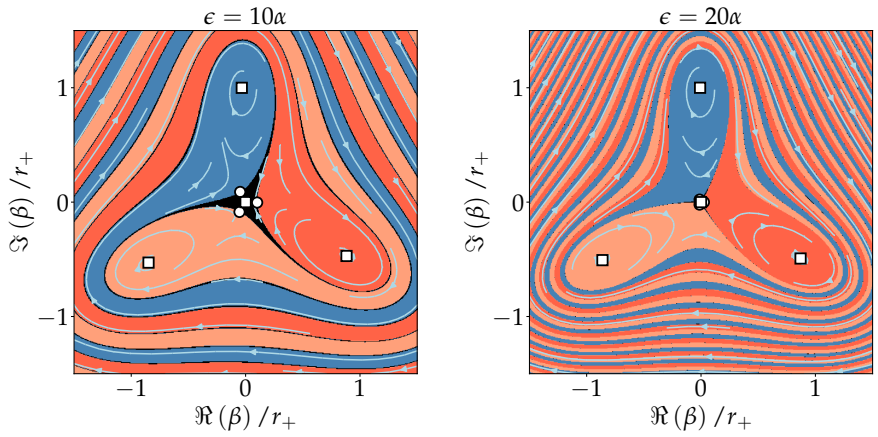

(a) (b)

Figure 3.2: Stability map of Eq. (3.1) represented in the complex plane with axis normalized by r_+ and for the parameters $\gamma = 10\alpha$, $\Delta = 0$ such as $\epsilon = 10\alpha$ (a), $\epsilon = 20\alpha$ (b). Each point represents a pair of initial conditions $(\Re[\beta(0)], \Im[\beta(0)])$ and the colour indicates the fixed point $\beta(t)$ converges to. Hence, only the stable fixed points have a corresponding colour. Additionally, these graphs contain a streamline plot (light blue), which indicates the dynamic of the system and furthermore, the fixed points are plotted analogously to Fig. 3.1.

independent of the driving strength ϵ.

Next, we analyze the rotation around the fixed points r_+, which we found in the last section. The calculation led to a frequency of $\omega = \sqrt{3}\epsilon^2/\alpha$, in the limit of small distances around r_+.

For further investigation, we numerically investigate the frequency near one of the outer fixed points r_+. For simplicity, we set $\gamma = 0$ to obtain closed trajectories, since the inward motion only depends on the dissipation. Note that the unstable fixed points vanish for $\gamma = 0$. This can be checked by substituting $\gamma = 0$ in Eq. (3.6), which yields $r_+ = \epsilon/\alpha$ and $r_- = 0$. Furthermore, since the system is symmetric under $2\pi/3$ rotations, the choice of ϕ_+ does not matter. Thus, we choose the most convenient case, which is given by the fixed point $(0, r_+)$[5].

To calculate the frequency we first have to choose the initial conditions. Due to the rotational symmetry, the logical choice is to start near the fixed point and increase the distance between this fixed point and the initial condition radially outward. Hence, the initial conditions lie on the imaginary axis. For further investigation, we are interested in the frequency dependence on this distance, which we define as

5 Note that the complex phase for this fixed point is exactly $\phi_+ = \pi/2$ due to Eq. (3.7).

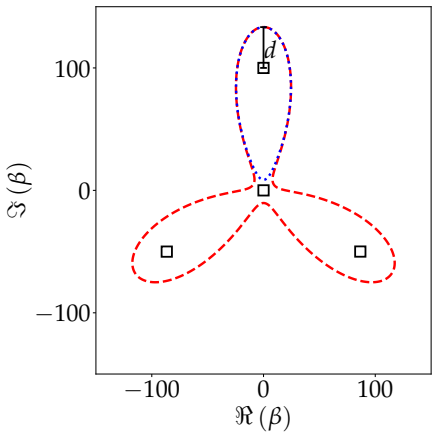

Demonstration of the closed trajectories for two different initial conditions near the transition. The distance between the investigated fixed point and the initial conditions is marked by the black line and the letter d. The blue dotted line represents a motion that circulates the upper fixed point. The initial conditions of the red dashed curve are slightly far away from the fixed point, *i. e.* they are described by a slightly larger value of d, resulting in a trajectory around all three fixed points.

Figure 3.3

$d \equiv \Im[\beta(0)] - r_+$, with the initial condition $\beta(0)$.

The resulting solution for $\beta(t)$ circulates the fixed point in a closed trajectory in the complex plane, which is visualized in Fig. 3.3. We obtain the period duration by checking when the real part of this trajectory becomes negative. The time required for this motion is one-half of the period duration T. Based on the resulting time, we can calculate the frequency via $\omega = 2\pi/T$. This process is repeated for multiple distances d, starting at $d = 0$ up to $d = r_+$.

Before presenting the results of this simulation, we first want to discuss what kind of behavior we expect. For small frequencies, we obtain the limit $\omega_{\text{lim}} = \sqrt{3}\epsilon^2/\alpha$ due to the analytical calculations. Further, we expect to observe a transition between the oscillation around the investigated fixed point and the oscillation around all three fixed points for large enough distances d. If d approaches this transition, the trajectory passes the point $r = 0$ increasingly closer but never reaches it because $r = 0$ is a fixed point. If we now assume there is an infinitesimally small point, as an initial condition, whose trajectory would separate the trajectories around one fixed point and all three fixed points, this trajectory would converge to $r = 0$. In this case, the trajectory would take an infinite amount of time to fulfill one period. Hence, the frequency would be zero at the transition.

In conclusion, we first expect a decreasing frequency that approaches zero with a diverging derivative[6] at the transition between the inner and the outer oscillations. After that we expect the frequency to in-

6 The frequency has a diverging derivative because the period duration approaches infinity at the transition and the frequency is given by $2\pi/T$

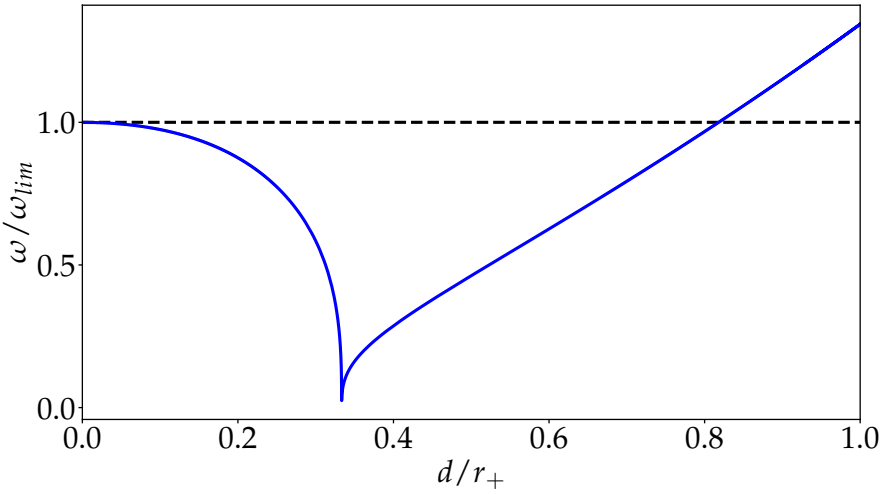

Figure 3.4: Oscillation frequency ω of a given trajectory, normalised by the frequency $\omega_{\text{lim}} = \sqrt{3}\epsilon^2/\alpha$, as a function of d/r_+, for $\gamma,\ \Delta = 0$ (blue). The black dashed line indicates the limit frequency ω_{lim}. The frequency ω does not reach zero at the transition because the period duration diverges to infinity at this point, so the resolution is limited by the simulation time of the numerical calculation. Due to the normalization, this curve is independent of the parameters ϵ and α.

crease again, but we do not have any predictions of the behavior.

In Fig. 3.4 the numerically calculated result is presented. In the limit $d/r_+ \to 0$ the frequency ω approaches ω_{lim} and at the transition, which is approximately at $d = 0.33r_+$, we find the diverging period duration. These results match our expectations, which we discussed earlier.

Further, we find a linear dependency of the distance d in the frequency ω after the transition, in the investigated region. At this point, we cannot make any predictions about the behavior of the frequency for $d \gg r_+$, we can only assume that the frequency continues to increase linearly.

However, it has to be emphasized that the behavior of the frequency ω strongly depends on γ in the region directly after the transition. For $\gamma \neq 0$ the solution for β would converge to the neighboring fixed point of r_+, as we can see in Fig. 3.2. Additionally, we expect to find similar behavior at any transition between the black and the colored regions. Besides these effects, we expect that Fig. 3.4 describes the frequency in regions that are not near a transition. Thus, in the limit $d \gg r_+$ we expect to find linearly increasing frequency, in those regions.

4

THE INFLUENCE OF THERMAL FLUCTUATIONS

4.1 PROPERTIES OF NOISE

4.1.1 *Characteristics of White Noise*

In the previous chapter, we investigated the system at zero temperature. To study the system at finite temperatures, we introduce thermal fluctuations. This leads to the extension of Eq. (3.1)

$$\dot{\beta} + (\gamma + i\Delta)\,\beta - \epsilon\overline{\beta}^2 + i\alpha\beta^2\overline{\beta} = \xi(t), \tag{4.1}$$

with the complex function $\xi(t) = \xi_R(t) + i\xi_I(t)$ that describes the noise. Before we start the examination of Eq. (4.1), we discuss the characteristics of noise in order to execute analytic calculations and numerical simulations. [11]

Since $\xi(t)$ is a complex function, the real and imaginary parts have to be considered separately. To treat the real and imaginary parts equally and not create a preferable direction, the real and imaginary parts of the noise have identical properties and are uncorrelated. Furthermore, the investigated noise is on average zero $\langle\xi(t)\rangle = 0$. In general, noise is characterized by the auto-correlation function $f(t,t')$

$$\left\langle \overline{\xi(t)}\xi(t') \right\rangle = f(t,t'), \tag{4.2}$$

where $\langle . \rangle$ represents the average over an ensemble of noise. The meaning of this definition can be illustrated with the following example. If we want to determine the average solution $\langle\beta(t)\rangle$ numerically, we first calculate an ensemble of solutions $\beta(t)$. Due to the noise, all obtained trajectories are different. Now, to receive $\langle\beta(t)\rangle$ we have to average over all solutions, *i. e.* for each time t we calculate the arithmetic average over the ensemble of all points at this time. Therefore, Eq. (4.2) describes the average of the amplitude squared of the noise at two times t and t'.

Further, the auto-correlation function $f(t,t')$ is defined as the Fourier transform of the spectral density $S(\omega)$

$$f(t,t') = \frac{1}{2\pi}\int_{-\infty}^{\infty} S(\omega)e^{-i\omega(t-t')}\,d\omega. \tag{4.3}$$

In this investigation, we consider white noise which has a constant spectral density. Thus, we define a new parameter κ which describes the strength of the thermal fluctuations, given by $S(\omega) = S(0) \equiv \kappa$. This leads to the auto-correlating function $f(t, t') = \kappa\delta(t - t')$, with the Dirac delta-function $\delta(t - t')$. Therefore, the auto-correlating function is zero for $t \neq t'$, which implies that the amplitude of the noise at time t does not depend on its history, *i. e.* it is independent of the noise at the time $t - dt$, for $dt > 0$.

We can summarize the characteristics of the considered white noise, which are necessary for the following calculations:

- $\left\langle \overline{\xi(t)}\xi(t') \right\rangle = \kappa\delta(t - t')$
- $\langle \xi(t) \rangle = \langle \xi_{R/I}(t) \rangle = 0$

4.1.2 *Fluctuation-Dissipation-Theorem*

For a better understanding of the physical meaning of κ, we derive the fluctuation-dissipation-theorem, which connects the dissipation γ with the thermal fluctuations κ.

Therefore, we investigate the system in thermal equilibrium such that the energy is given by the fluctuations. This implies that we consider oscillations around the origin $\beta = 0$ in which the driving and stabilizing strength have a negligible small influence. In thermal equilibrium, the energy is given by the equipartition theorem[10], which leads to $E_{\text{eq}} = fk_BT/2 = k_BT$, with the Boltzmann constant k_B, the absolute temperature T, and the degrees of freedom f. Since we study a one-dimensional oscillator, the system has two degrees of freedom—the kinetic and potential energy.

In order to associate the energy in thermal equilibrium with a quantity of the system, we first define the energy of the system without fluctuations. As we already introduced in Sec. 2.1, the energy of the system is given by the sum of kinetic and potential energy. Therefore, if the system only has potential energy, the oscillation amplitude takes its maximum and the total energy is given by $E = E_s|\tilde{\beta}|^2 + E_q|\tilde{\beta}|^4$, where $|\tilde{\beta}|$ is the maxmimum oscillation amplitude and E_s such as E_q are constants which define the energy scales of the system.[1] Since we investigate the system for small fluctuations around the origin, we can neglect the quartic term, which leads to $E \approx E_s|\tilde{\beta}|^2$.

To include the noise, we now consider β as a solution of Eq. (4.1) and average the energy $\langle E \rangle$ to take thermal fluctuations into account.

1 Here, the tilde is used to clearly differentiate between classical solution and the solution which includes noise.

Furthermore, we have to consider the limit $t \to \infty$ to obtain a state of equilibrium. Hence, the energy in thermal equilibrium is given by $E_{\text{eq}} \approx \lim_{t\to\infty} E_s \left\langle |\beta|^2 \right\rangle$.

To calculate $\left\langle |\beta|^2 \right\rangle$, we investigate the simplified differential equation, in which we set $\alpha, \epsilon = 0$ since these terms have a negligible small influence. Thus, we obtain the following differential equation with the general solution $\beta(t)$

$$\begin{aligned} &\dot{\beta} + \chi\beta = \xi, && \chi \equiv \gamma + i\Delta \\ &\beta(t) = \left(\int_0^t \xi(t') e^{\chi t'} \, dt' + \beta_0 \right) e^{-\chi t}. \end{aligned} \tag{4.4}$$

At this point, we can see that the average solution $\langle\beta\rangle$ corresponds to a solution without thermal noise[2]. This finding is based on the fact that the noise itself is on average zero, so the solution $\beta(t)$ describes random fluctuations around the path at zero temperature. A good way to explain the effect of the noise ξ is the following analogue. ξ is like a force pulling or pushing β randomly back and forth. Since the strength and direction of the force is random, it is possible to obtain completely new paths, even from one stable fixed point to another. Nevertheless, if we average over all possible trajectories of β, we obtain the trajectory without noise.

Now, we continue with the calculation of $\left\langle |\beta|^2 \right\rangle$ to achieve the energy in thermal equilibrium. This calculation leads to

$$\left\langle |\beta|^2 \right\rangle = \frac{\kappa}{2\gamma} \left[1 + e^{-2\gamma t} \left(\frac{2\gamma}{\kappa} |\beta_0|^2 - 1 \right) \right]. \tag{4.5}$$

Here we can see that in the limit $t \to \infty$, which describes the state of thermal equilibrium, only the first term remains. To develop a better understanding of what this physically means, it is beneficial to calculate the variance of β, which is given by

$$Var(\beta) = \left\langle |\beta|^2 \right\rangle - \left\langle \overline{\beta} \right\rangle \langle \beta \rangle = \frac{\kappa}{2\gamma} \left(1 - e^{-2\gamma t} \right). \tag{4.6}$$

The second term of the variance vanishes in the limit $t \to \infty$ due to the form of the solution in Eq. (4.4). Thus, the variance in thermal equilibrium is given by

$$\lim_{t\to\infty} Var(\beta) = \frac{\kappa}{2\gamma}. \tag{4.7}$$

Therefore, the calculated result shows that the width of the distribution of β is proportional to the strength of the noise κ and inverse proportional to the dissipation γ. Thus, for increasingly strong damping γ

2 Note that we assume for simplicity that we can interchange the average operation $< . >$ with the integral.

in comparison to the fluctuations κ, the trajectory of β fluctuates very little around the origin in the complex plane because each excitement by the fluctuations results in a quickly decreasing oscillation amplitude due to the high energy loss. This argument works analogously in the case of large fluctuations resulting in a larger variance. Thus, the result of the variance of β matches the physical understanding and expectations of a system that contains fluctuations.

However, based on the result in Eq. (4.5), we finally can determine the energy in thermal equilibrium. By comparing this result to $E_{\mathrm{Eq}} = k_B T$, we obtain the fluctuation-dissipation theorem

$$\kappa = 2\gamma \frac{k_B T}{E_s} \tag{4.8}$$

This equation connects the fluctuations described by κ and the dissipation γ. Furthermore, we can see that κ is proportional to the ratio of the thermal energy $k_B T$ and the energy scale of the system E_s for small oscillation amplitudes.

A qualitative example of this theorem is Johnson noise in a resistor. A current in a resistor creates heat due to the dissipation, which can be described by fluctuating particles such that dissipation leads to fluctuations. However, this also works the other way around. If we consider a circuit at a finite temperature which is not connected to a voltage source, we are able to measure a current due to thermal fluctuations of the electrons and atoms. So in this case, the thermal fluctuations convert heat into electrical energy, which is the inverse of dissipation. [12]

4.2 BROWNIAN MOTION

Before we analyze the influence of the noise analytically and numerically, we first introduce the discrete properties of the noise and a method to numerically solve Eq. (4.1).

Analogous to the previous section, we analyze the system in its simplest form in order to determine the discrete properties of the noise. Therefore, we investigate the system at $r = 0$, study how the variance of β changes over time, and compare the result to the continuous calculations, which lead to Eq. (4.6). Therefore, we obtain the differential equation

$$\dot{\beta} = \xi. \tag{4.9}$$

This equation is a realization of Brownian motion, which describes the random movement of molecules due to thermal fluctuations [6]. Further, this representation of the Brownian motion is known as a random walk—in our case in two dimensions since β and ξ are complex

functions—which describes random movements due to the noise ξ.

To analyze the Brownian motion we write this equation in a discrete form by using the Euler-forward-method which defines the derivative of a discrete function as follows

$$\dot{\beta}_n = \frac{\beta_{n+1} - \beta_n}{\Delta t}\,, \qquad \Delta t > 0 \quad \text{and} \quad n \in \mathbb{N}_0. \tag{4.10}$$

Hence, the discrete form of Eq. (4.9) results in a recursive series, given by

$$\beta_{n+1} = \beta_n + \Delta t \cdot \xi_n. \tag{4.11}$$

The solution of this recursive series is given by

$$\begin{aligned} \beta_n &= \Delta t \cdot \sum_{i=1}^{n} \xi_i\,, \qquad\qquad n > 0 \\ \beta_0 &= 0, \end{aligned} \tag{4.12}$$

which describes the expected random walk. Each step of β is a given by a particular realization of the fluctuations ξ_n modulated by the time step Δt, resulting in a sum of random steps. In general, to describe the discrete noise of thermal fluctuations a Gaussian distribution with variance $Var(\xi_n) = \sigma^2$ is used. Thus, each summand ξ_n is a random Gaussian distributed value.

Furthermore, we proceed similar to Sec. 4.1 and determine the variance of β_n by calculating $\beta_n\overline{\beta_n}$ and take the average $\langle . \rangle$.[3] This calculation yields

$$Var(\beta_n) = n\Delta t^2\sigma^2. \tag{4.13}$$

Since n describes the number of time steps, we can substitute $n = t/\Delta t$ and ultimately obtain

$$Var(\beta_n) = Dt\,, \qquad\qquad D \equiv \Delta t \cdot \sigma^2. \tag{4.14}$$

By comparing this result with equation Eq. (4.6) in the limit $t \to 0$, we find the variance of the noise

$$\left\langle \xi_i \overline{\xi_j} \right\rangle = Var(\xi_i)\delta_{ij} = \sigma^2\delta_{ij} = \frac{\kappa}{\Delta t}\delta_{ij}. \tag{4.15}$$

Since the noise ξ_n is a complex random variable, it can be written as $\xi_n = \xi_{R,n} + i\xi_{I,n}$, where $\xi_{R/I,n} \in \mathbb{R}$ are two independent, uncorrelated random variables with identical properties. Thus, we obtain the variance for the real and imaginary parts of the noise

$$Var(\xi_{R/I,n}) = \tilde{\sigma}^2 = \frac{\kappa}{2\Delta t}. \tag{4.16}$$

This result is used to derive the action and simulate the noise numerically.

3 Note that the average of β_n is zero due to the characteristics of the noise.

4.3 ANALYSIS OF THE TUNNELING RATE

4.3.1 *Stability Maps with Thermal Fluctuations*

After having characterized the properties of the noise, we investigate how the noise influences the system. Therefore, we come back to the stability maps we introduced in Sec. 3.3 and additionally consider fluctuations at a finite temperature.

To bring the influence of the noise in the foreground, we do not include the streamline plot and the fixed points. In Fig. 4.1a we can see the case of a small thermal energy $k_B T = 10^{-3} E_s/2$. Here, the black lines which separate the colored regions are slightly irregular in comparison to Fig. 3.2a. The effect of the noise is most visible in the regions far away from the origin. In these regions, the black lines are at some points more dense than at other points. However, the overall effects are light and the system does not change much in the regime of this strength of noise.

As a contrast, Fig. 4.1b presents thermal fluctuations which are two orders of magnitude greater than in the previous case. Here, the black lines dissolve and change into randomly distributed black dots around the originally solid black line. Thus, between the different regions emerges a transition, so these regions are no longer clearly separated from each other. This effect increases for increasing distances from the origin because the width of the black lines and colored regions decreases. Hence, in the limit $|\beta| \gg r_+$, the influence of the black lines vanish and the three colored regions completely merge together. This results in non-deterministic behavior, such that each of the three outer fixed points has the probability of $1/3$ that the initial condition $|\beta_0| \gg r_+$ leads to a trajectory that converges to the considered fixed point.

Furthermore, these maps introduce the concept of tunneling due to thermal fluctuations. Let us consider the fixed point $r = 0$ in thermal equilibrium, as we discussed in Sec. 4.1. There is a probability that the solution β overcomes the potential barrier of the inner fixed point and, thus, ends up at one of the outer fixed points, analogous to quantum tunneling. This process can be very unlikely to happen, depending on the intensity of the noise, and is, therefore, not directly observable in the stability maps. However, such a tunneling event can be characterized by an average tunneling time which describes the average time a solution β requires to escape the barrier between two stable fixed points. Therefore, the stability maps in Fig. 4.1 depend on the coding process which was used to create them.

To better understand the dependence of the computation process, we discuss two different approaches to create a stability map that includes noise. Further, we consider the Euler-forward-method, which results in a recursive series that is computed numerically, to solve Eq. (4.1). This process will be discussed in detail in Sec. 4.4.

The first kind of computation consists of two parallel processes. The first process numerically determines the current value of the solution β_n, while the second process locates this value in the complex plane. As soon as the solution enters a certain region, which is assigned to one of the stable fixed points, the simulation is stopped and the respective color is assigned. This implies that the simulation time is not a fixed parameter. The second variant, which was used to create Fig. 4.1, uses a fixed simulation time for which Eq. (4.1) is solved. This means that the solution β, represented as an array, has for each initial condition the same number of entries and between every entry, the same small step in time Δt is used. In this case, the simulation time plays an important role since we expect to find a larger tunneling events for longer simulation times.

Let us consider the example where the tunneling rate of the fixed point $r = 0$ is negligibly small compared to the tunneling rate of the outer fixed points r_+. In this scenario, the black regions would vanish

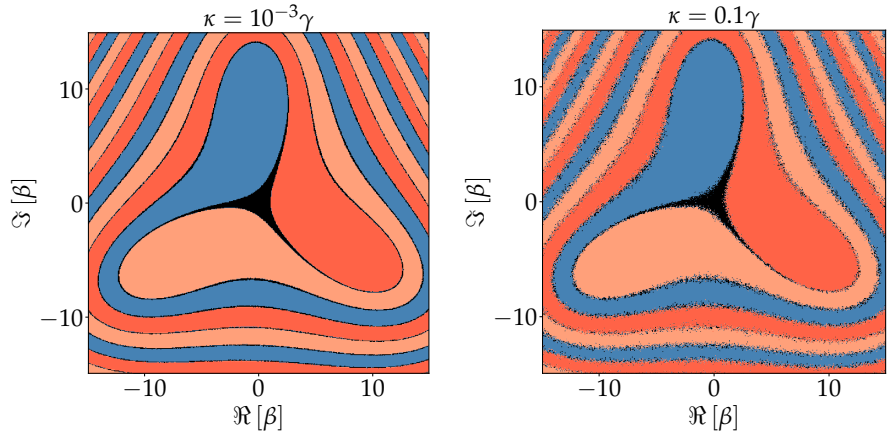

Figure 4.1: Stability maps at two different finite temperatures for the parameter $\Delta = 0$, $\epsilon = 10\alpha$, $\gamma = 10\alpha$ such as $\kappa = 10^{-3}\gamma$ (a) and $\kappa = 0.1\gamma$ (b). These maps were analogously created to Fig. 3.2; Each pixel represents an initial condition and the color indicates to which fixed point the solution $\beta(t)$ of Eq. (4.1) converges. Each solution was calculated for the same simulation time $t \approx 30T$, where T is the limit of the period duration we discussed in Sec. 3.3. Furthermore, since the noise is random each stability map only shows the influence of the noise but it cannot be exactly reproduced.

in the limit of an infinite simulation time because the tunneling process happens mostly in one direction; from the inside—black regions—to the outside—colored regions. However, it has to be emphasized that this scenario would not show a wrong representation of the system, it rather has to be considered as an additional physical factor that is a part of the stability map.

Figure 4.1 represents fluctuation for a moderate simulation time such that black lines appear blurred but they do not vanish. It is necessary to simulate the solution for a long enough time such that each initial condition can be reasonably assigned to one of the fixed points. *E. g.* the trajectories need increasingly more time to pass a fixed point as the distance to this fixed point decreases which we discussed in Sec. 3.3. This includes the unstable fixed points r_-, which are passed by some trajectories that lead to the center as well as some trajectories which lead to the outer fixed points r_+. However, this simulating time is in a regime such that the tunneling events are very unlikely to happen, which we can see in Fig. 4.1b since the larger areas are mostly maintained.

4.3.2 *Description by the Action*

This subsection is inspired by the notes *A short tutorial on the path integral formalism for stochastic differential equations* by Dani Martí to derive the action and the book *Many-Body Theory of Non-Equilibrium Systems* by Alex Kamenev to solve the saddle-point equations. [7][8]

Now, we derive the tunneling rate mathematically based on the path integral formalism. Therefore, we first recall the Hamiltonian principle and recall the definition of the action which is used in classical mechanics. Afterwards, we introduce the path integral formalism and derive the corresponding action for Eq. (4.1).

Firstly, the Hamiltonian principle—also called the principle of least action—states that a physical system behaves in such a way that the variation of the action S is stationary. The mathematical description of this principle is given by

$$\delta S[q, p] = 0. \tag{4.17}$$

The action $S[q, p]$ is a functional[4] —denoted by the square brackets—of the canonical coordinate q and the canonical momentum p, which satisfy the Hamiltonian equations. Originally, the action is defined via

4 A functional is a function that depends on a function and outputs a scalar. *E. g.* an integral is a functional.

the Lagrange function $\mathcal{L}$, but we focus on the representation via the Hamiltonian $\mathcal{H}$

$$S[q,p] = \int_{t_1}^{t_2} dt\ p\dot{q} - \mathcal{H}(q,p), \tag{4.18}$$

which is equivalent since the Lagrangian and the Hamiltonian are connected by a Legendre transformation.

Further, the δ-variation describes the differential of a functional, which considers different paths of $p(t)$ and $q(t)$ in the phase space at a fixed time. However, the initial and endpoints stay fixed. The differential acts on Eq. (4.18) as follows

$$\begin{aligned}
\delta S[q,p] &= \delta \int_{t_1}^{t_2} dt\ p\dot{q} - \mathcal{H}(q,p) \\
&= \int_{t_1}^{t_2} dt\ \left(\frac{\partial(p\dot{q})}{\partial p} - \frac{\partial \mathcal{H}(q,p)}{\partial p}\right)\delta p + \left(\frac{\partial(p\dot{q})}{\partial q} - \frac{\partial \mathcal{H}(q,p)}{\partial q}\right)\delta q \\
&= \int_{t_1}^{t_2} dt\ \left(\dot{q} - \frac{\partial \mathcal{H}(q,p)}{\partial p}\right)\delta p + \left(-\dot{p} - \frac{\partial \mathcal{H}(q,p)}{\partial q}\right)\delta q.
\end{aligned} \tag{4.19}$$

To obtain the result in the third line we partially integrated the term $\partial(p\dot{q})/\partial q = p\ (\partial\dot{q}/\partial q)$ where the terms of the initial and end terms are zero since these points are not varied. [9]

Furthermore, the terms in the brackets have to be independently zero to satisfy Eq. (4.17), which results in the Hamiltonian equations. This brief recapitulation of the classical action shows that the principle of least action is equivalent to the Hamiltonian equations. In general, $\delta S = 0$ describes the saddle-point equations which have to be satisfied to minimize the action.

In 1942, Richard Feynman reformulated the path integral formalism as a new formulation of quantum mechanics.[5]

Now, we introduce the path integral formalism and give a brief overview of what the goal of the following computation is.

The path integral formalism was first introduced by Norbert Wiener in 1920 to solve problems considering the theory of diffusion and Brownian motion. In comparison, in classical mechanics, the movement of a particle between two points is described by one trajectory, while the path integral formalism considers every possible trajectory between these points weighted with a certain probability. While the classical trajectory is given by the least action, this formulation considers this path to be the most probable but it is not the only possible

path the particle can take [5]. This can be described by the probability density functional[5]

$$P[x(t)|x_0] = \int \mathcal{D}\tilde{x}(t)\, e^{-S[x,\tilde{x}]}, \tag{4.20}$$

where $\tilde{x}$ describes the non-classical behavior of the system due to the thermal fluctuations and $\mathcal{D}\tilde{x}(t)$ describes the integration over all possible paths. Both of these terms are further discussed in the following derivation. Furthermore, this definition of the action is motivated by the exponential dependence of $-S$. Since we are interested in the path with the greatest contribution which is given by the minimal action, we obtain $\delta S[\beta, \tilde{\beta}_R, \tilde{\beta}_I] = 0$, while the contribution of the other possible paths are exponentially suppressed.

Every physical field has a corresponding action, whose saddle-point equations lead to the description of the system. For example, the principle of least action in electrodynamics leads to the Maxwell equations, or in general relativity, the corresponding action leads to Einstein's field equations. [3][13]

In order to derive the probability density functional, we start by rewriting Eq. (4.1) in a more general form, which also provides a more clear overview. In general, stochastic processes can be described by the Langevin equation

$$\dot{\beta} = f(\beta) + \xi, \quad f(\beta) := -\chi\beta + \epsilon\overline{\beta}^2 - i\alpha\beta^2\overline{\beta}. \tag{4.21}$$

The Langevin equation describes systems that have deterministic processes—$f(\beta, t)$—and, additionally, non-deterministic processes such as thermal fluctuations.

For further analysis, we change to the discrete representation of the system because it simplifies the calculations with the noise. We rewrite Eq. (4.21) by using the Euler-forward-method and obtain

$$\beta_{n+1} - \beta_n - f(\beta_n)\Delta t - \xi_n \Delta t - \beta_0 \delta_{n0} =: Z_n = 0, \tag{4.22}$$

where δ_{n0} is the Kronecker delta and β_0 is the initial condition. Since we investigate the fixed point $r = 0$ the initial condition is given by $\beta_0 = 0$. Furthermore, we define this equation as $Z_n = Z_{R,n} + iZ_{I,n}$, in which the real and imaginary parts have to be zero independently, which are denoted by R/I.

Further, to obtain the probability density functional we first define the joint probability density functional for a complex stochastic differential equation, which is given by

$$P(\beta|\xi;\beta_0) = \prod_{n=0}^{N} \delta\left(Z_{R,n}\right) \delta\left(Z_{I,n}\right), \tag{4.23}$$

where $x = \{x_0, x_1, ..., x_N\}$, $\xi = \{\xi_0, \xi_1, ..., \xi_N\}$, and the number of steps $N = T/\Delta t$. This joint probability density functional encodes

5 Note that this case describes a one-dimensional system which is used for illustration. The system described by Eq. (4.1) is two-dimensional since it is a complex differential equation, which results in two path integrals.

the differential equation at every point for particular realization of the noise ξ. Furthermore, Eq. (4.23) can be expressed by the Fourier transform of the delta function

$$P(\beta|\xi;\beta_0) = \int_{-\infty}^{\infty}\int_{-\infty}^{\infty}\prod_{n=0}^{N}\frac{dk_{R,n}}{2\pi}\,\frac{dk_{I,n}}{2\pi}\exp\left[-i\left(k_{R,n}Z_{R,n}+k_{I,n}Z_{I,n}\right)\right],$$

which we use in the following computations.

Since the goal is to obtain the probability density functional, the next step is to calculate the joint probability density function $P(x|x_0)$, which we obtain by integrating the noise ξ_n over each realization of Eq. (4.23) modulated by the probability density $p(\xi_{R/I,n})$ of the noise. Since we investigate complex noise, we have to integrate over the real and imaginary parts of ξ separately.

$$P(\beta|\beta_0) = \int\int P(x|\xi;x_0)\prod_{n=0}^{N}p(\xi_{R,n})p(\xi_{I,n})\,d\xi_{R,n}\,d\xi_{I,n} \tag{4.24}$$

As we already proposed in Sec. 4.2, the discrete noise $\xi_{R/I,n}$ are realized as Gaussian distributed random variables with variance $Var(\xi_{R/I,n}) = \tilde{\sigma}^2 = \kappa/2\Delta t$. Therefore, the probability density is given by

$$p(\xi_{R/I,n}) = \frac{1}{\sqrt{2\pi\tilde{\sigma}^2}}\exp\left(-\frac{\xi_{R/I,n}^2}{2\tilde{\sigma}^2}\right). \tag{4.25}$$

To maintain a clear overview of the derivation, we define the new variables $X_{R/I,n} \in \mathbb{R}$ via

$$X_n := X_{R,n} + iX_{I,n} := \frac{\beta_{n+1}-\beta_n}{\Delta t} - f(\beta_n). \tag{4.26}$$

Based on this definition we can rewrite equation Eq. (4.22) as $Z_n = X_n\Delta t - \xi_n\Delta t$. In this definition we separate the deterministic term $X_n\Delta t$ and the thermal fluctuations $\xi_n\Delta t$. Since X_n does not depend on the noise we can interchange the integration over $\xi_{R/I,n}$ and the terms which only depend on $X_{R/I,n}$ in Eq. (4.24).

Hence, we obtain the following form of the joint probability density function

$$
\begin{aligned}
P(\beta|\beta_0) = &\int \prod_{n=0}^{N} \frac{dk_{R,n}}{2\pi} \exp\left(-ik_{R,n}X_{R,n}\Delta t\right) \int \prod_{n=0}^{N} \frac{d\xi_{R,n}}{\sqrt{2\pi\tilde{\sigma}^2}} \exp\left(-\frac{\xi_{R,n}^2}{2\tilde{\sigma}^2} + ik_{R,n}\xi_{R,n}\Delta t\right) \\
&\times \int \prod_{n=0}^{N} \frac{dk_{I,n}}{2\pi} \exp\left(-ik_{I,n}X_{I,n}\Delta t\right) \underbrace{\int \prod_{n=0}^{N} \frac{d\xi_{I,n}}{\sqrt{2\pi\tilde{\sigma}^2}} \exp\left(-\frac{\xi_{I,n}^2}{2\tilde{\sigma}^2} + ik_{I,n}\xi_{I,n}\Delta t\right)}_{=\prod_{n=0}^{N} \exp\left(\frac{\tilde{\sigma}^2 \left(ik_{I,n}\right)^2}{2}\Delta t^2\right)} \\
= &\int \prod_{n=0}^{N} \left(\frac{d\tilde{\beta}_{R,n}}{2\pi i}\right) \exp\left[-\Delta t \sum_{n=0}^{N} \left(\tilde{\beta}_{R,n}X_{R,n} - \frac{\kappa\tilde{\beta}_{R,n}^2}{4}\right)\right] \\
&\times \int \prod_{n=0}^{N} \left(\frac{d\tilde{\beta}_{I,n}}{2\pi i}\right) \exp\left[-\Delta t \sum_{n=0}^{N} \left(\tilde{\beta}_{I,n}X_{I,n} - \frac{\kappa\tilde{\beta}_{I,n}^2}{4}\right)\right],
\end{aligned}
$$

where we solved the integration over $d\xi_{R/I,n}$ at the first equal sign by completing the square and after the second equal sign we used the substitution $\tilde{\beta}_{R/I,n} \equiv ik_{R/I,n}$.

In the last step, we go back to the continuous limit $N \to \infty$ and $\Delta t \to 0$, such that $T = N\Delta t$ stays constant. Therefore, we use the following definitions

$$
\begin{aligned}
\Delta t \sum_{n=0}^{N} &\longrightarrow \int_0^T dt \\
\int \prod_{n=0}^{N} \frac{d\tilde{\beta}_{R/I,n}}{2\pi i} &\longrightarrow \int \mathcal{D}\tilde{\beta}_{R/I}(t) \\
X_n &\longrightarrow X(t) = \dot{\beta}(t) - f\left(\beta(t)\right) \\
\tilde{\beta}_{R/I,n} &\longrightarrow \tilde{\beta}_{R/I}(t)
\end{aligned}
\tag{4.27}
$$

where we can now explicitly see how the path integration over $\mathcal{D}\tilde{\beta}_R$ is defined.

In this limit, we obtain the probability density functional

$$
P[\beta|\beta_0] = \int\int \mathcal{D}\tilde{\beta}_R \, \mathcal{D}\tilde{\beta}_I \exp(-S\left[\beta, \tilde{\beta}_R, \tilde{\beta}_I\right]) \tag{4.28}
$$

where we define the action

$$
\begin{aligned}
S\left[\beta, \tilde{\beta}_R, \tilde{\beta}_I\right] = \int_0^T dt \; &\tilde{\beta}_R \left[\dot{\beta}_R - f_R(\beta_R, \beta_I)\right] - \frac{\kappa\tilde{\beta}_R^2}{4} \\
&+ \tilde{\beta}_I \left[\dot{\beta}_I - f_I(\beta_R, \beta_I)\right] - \frac{\kappa\tilde{\beta}_I^2}{4},
\end{aligned}
\tag{4.29}
$$

where $\beta_{R/I}$ and $f_{R/I}(\beta_R, \beta_i)$ are the real- and imaginary parts of β and $f(\beta)$, respectively.

For the further investigation, we introduce the vectors $\mathbf{q} \equiv (q_x, q_y) \equiv (\beta_R, \beta_I)$, $\mathbf{p} \equiv (p_x, p_y) \equiv (\tilde{\beta}_R, \tilde{\beta}_I)$, and $\mathbf{f} \equiv (f_R, f_I)$, where $q_{x/y}$ describe the coordinates in the complex plane of the system and $p_{x/y}$ encodes the noise. We choose this representation to emphasize that we can express the action analogously to the action in classical mechanics given by Eq. (4.18), but in this case, in two dimensions. The action as well as the corresponding fictitious Hamiltonian are given by

$$\begin{aligned} S[\mathbf{q}, \mathbf{p}] &= \int_0^T dt\ \mathbf{p} \cdot \dot{\mathbf{q}} - \mathcal{H}(\mathbf{q}, \mathbf{p}), \\ \mathcal{H}(\mathbf{q}, \mathbf{p}) &= \mathbf{p} \cdot \mathbf{f}(q_x, q_y) + \frac{\kappa |\mathbf{p}|^2}{4} \end{aligned} \tag{4.30}$$

and the saddle-point equations are given by the Hamiltonian equations

$$\dot{q}_k = \frac{\partial \mathcal{H}}{\partial p_k}, \quad -\dot{p}_k = \frac{\partial \mathcal{H}}{\partial q_k}, \quad k \in \{x, y\} \tag{4.31}$$

After this derivation, we can start with the calculation of the tunneling rate. First of all, we discuss what behavior to expect. To this end, we revisit the stability map in Fig. 3.2a from Ch. 3. In this figure, we can see that the shortest possible distance between $r = 0$ and any colored region is given by the fixed points r_-. Therefore, we expect that the escape over the potential barrier is most probable over the unstable fixed points. Based on this idea we can define a tunneling event at $r = 0$.

A tunneling event from the inner fixed point $r = 0$ to one of the outer fixed points r_+ occurs if the trajectory β reaches a point beyond r_-, i. e. *$|\beta| > r_-$, and, therefore, a point beyond the potential barrier.*

Furthermore, we can make three simplifications for this problem. Firstly, we neglect the stabilizing strength, *i. e.* $\alpha = 0$. In this approximation, the unstable fixed points r_- are given by the first order of Eq. (3.4) and the outer fixed points r_+ are undefined, resulting in a diverging oscillation amplitude for $|\beta| > r_-$ since the system is no longer stabilized. However, this description of the system is sufficient because we are only interested in the region around the center up to r_-. Secondly, we neglect the detuning $\Delta = 0$, so we do not take the rotation around $r = 0$ into account. Finally, we use the rotational symmetry to our advantage by only investigating the most simple unstable fixed point $\beta = r_-$. Since we set $\alpha = 0$ this unstable fixed point lies exactly on the real axis. Therefore, the noise in the imaginary direction, described by p_y, has no influence on the tunneling rate

over this point, so we set $p_y = 0$. Furthermore, the classical trajectory between the considered fixed points lies on the real axis, which can be seen in the stability plots of Ch. 3.3 in Fig. 3.1b. Hence, we further set $q_y = 0$. After finding the solutions for q_x and p_x we have to confirm that these assumptions satisfy the saddle-point equations.

For these approximations, we obtain the following fictitious Hamiltonian and saddle-point equations

$$\begin{aligned} \mathcal{H} &= p_x f_R(q_x) + \frac{\kappa p_x^2}{4} = p_x(-\gamma q_x + \epsilon q_x^2) + \frac{\kappa p_x^2}{4} \\ \dot{q}_x &= -\gamma q_x + \epsilon q_x^2 + \frac{\kappa p_x}{2} \\ \dot{p}_x &= p_x\left(-\gamma + 2\epsilon q_x\right). \end{aligned} \tag{4.32}$$

These equations yield the classical case for $p_x = 0$. Since p_x encodes the noise, this matches our physical understanding.

At this point, the trick of rewriting the equations in the form of the Hamiltonian action leads to an advantage. The saddle-point equations conserve the Hamiltonian, *i.e.* $d\mathcal{H}/dt = 0$, which leaves the Hamiltonian constant. Hence, we investigate Eq. (4.32) and find two lines where the Hamiltonian is zero and, therefore, constant. The first solution is the trivial case $p_x = 0$, which describes the classical system. Therefore, this solution is not able to describe the escape over the potential barrier. However, the second line is given by $p_x = -4q_x(\gamma - \epsilon q_x)/\kappa$, which describes the non-classical case where the noise—described by p_x—creates a tunneling event. It is easy to check that this solution solves the saddle-point equations.

In addition to that, we have to check if the solution $p_x(q_x)$ also satisfies Eq. (4.31) and leads to the solutions $p_y, q_y = 0$, which we assumed to find. Indeed, we find an exponential dependence for q_y, which is zero for the initial condition $q_{y,0} = 0$ and for the variable p_y the solution is constant, which also vanishes for the initial condition $p_{y,0} = 0$. Therefore, the assumption led to the correct description of the system.

Furthermore, due to the form of the action and $\mathcal{H} = 0$, it is beneficial to rewrite the integral as an integration over the variable q_x. Therefore, we do not have to determine the explicit forms of $p_x(t)$ and $q_x(t)$. Hence, we can calculate the action

$$S = \int_0^T dt\ p_x \dot{q}_x = \int_0^{r_-} dq_x\ p_x(q_x) = \frac{r_-^2}{3}\frac{2\gamma}{\kappa} = \frac{1}{3}\frac{E_-}{k_B T}. \tag{4.33}$$

Here, the threshold energy $E_- = E_s r_-^2$ describes the oscillation energy at the unstable fixed points with amplitude r_-, which leads to a

more clear representation of the result.

Finally, we introduce the tunneling rate Γ_0, which is a probability per unit of time. Γ_0 is, to an exponential accuracy, given by the path with the greatest contribution to the path integral in Eq. (4.28). Thus, we obtain

$$\Gamma_0 \propto e^{-\frac{2}{3}\frac{\gamma r_-^2}{\kappa}} = e^{-\frac{1}{3}\frac{E_-}{k_B T}}. \tag{4.34}$$

This results matches the findings of the paper of Ref. [2], in which Josephson parametric down-conversion is studied. This system shows similar behavior to the parametrically driven Duffing-oscillator in the region of small oscillation amplitudes $|\beta| \leq r_-$.

Furthermore, we can determine the average tunneling time τ to an exponential accuracy, since $\tau \propto \Gamma_0^{-1}$. Hence, the average tunneling time has the following proportionality

$$\tau \propto e^{\frac{2}{3}\frac{\gamma r_-^2}{\kappa}} = e^{\frac{1}{3}\frac{E_-}{k_B T}}. \tag{4.35}$$

To physically understand this results, we discuss the limits of small and large temperatures.

The limit of small temperatures is described by $E_-/k_BT \gg 1$ such that the average tunneling time τ is very large. This can be physically motivated. For small fluctuations, we expect that a tunneling event is very unlikely since the potential barrier large in comparison to the thermal energy.

In the second limit, $E_-/k_BT \ll 1$, the thermal fluctuations are much larger than the potential barrier, resulting in a very short tunneling time.

4.4 SIMULATION OF THE TUNNELING RATE

In order to check the obtained results, we numerically investigate the system, simulate the tunneling process, and finally determine the tunneling rate. To reproduce the analytical result we have to neglect the detuning, *i.e.* $\Delta = 0$, since we expect that the rotation around the origin influences the tunneling rate. However, we do not neglect the stabilizing strength α in the numerical simulation to check if the approximation we made was reasonable.

At first, to calculate the tunneling rate we recall the definition of a tunneling event of the previous section. A tunneling event occurs if the numerically calculated solution β_n reaches a distance which is greater than the unstable fixed point r_-, *i.e.* $|\beta_n| > r_-$.

After this recapitulation, we discuss how we numerically solve Eq. (4.1) and realize the noise. In Sec. 4.2, we introduced the Euler-forward-method such that we rewrite the differential equation as a recursive series of the form

$$\beta_{n+1} = \beta_n + \xi_n \Delta t - \Delta t \left(\gamma \beta_n - \epsilon \overline{\beta}_n^2 + i\alpha \beta_n^2 \overline{\beta}_n \right). \tag{4.36}$$

The realisation of the noise $\xi_n = \xi_{R,n} + i\xi_{I,n}$ is given by the Gaussian distribution of the real and imaginary parts with the average $\langle \xi_{R/I,n} \rangle = 0$ and the variance $Var(\xi_{R/I,n}) = \kappa/2\Delta t$, which also was derived in this Sec. 4.2. Furthermore, to solve the recursive series we first have to choose initial conditions. Since we investigate the origin $r = 0$ of the system in thermal equilibrium, the initial conditions are also Gaussian distributed with the variance $Var(\beta_n) = \kappa/2\gamma$, as we derived in Sec. 4.1.

Furthermore, to obtain the correct description of the system, the time step Δt has to be less than the parameter which causes the fastest change in time of the system. In the region around the origin, the classical system converges with $e^{-\gamma t}$ to zero, which implies that γ is decisive for the change of rate of β. Therefore, to obtain a reasonable solution in this regime we find $\gamma \Delta t \ll 1$.

Now, we solve Eq. (4.36) and determine the tunneling time for a particular realization of β_n. This computation consists of two parallel

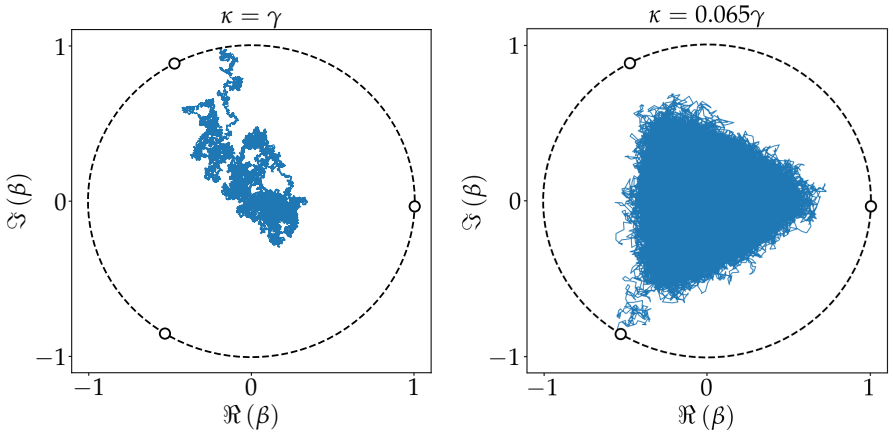

(a) (b)

Figure 4.2: Visualisation of the tunneling process by solving Eq. (4.36) for the parameters $\epsilon = 10\alpha$, $\gamma = 10\alpha$, $\Delta = 0$ and two different temperatures; $\kappa = \gamma$ (a) and $\kappa = 6.5 \cdot 10^{-2}\gamma$. In Fig. (a), a time step of $\Delta t = 10^{-3}/\gamma$ was used, while Fig. (b) was created with a time step of $\Delta t = 10^{-2}/\gamma$ and additionally only every second step of the solution was considered in order to reduce the amounts of data. Furthermore, these plots contain the unstable fixed points (black circles) and a black dashed line which marks the barrier $|\beta_n| = r_-$.

processes, similar to the alternative creation process of the stability map we discussed. In the first process, Eq. (4.36) is iteratively solved via python for a random initial condition, and for each step, a new realization of the noise ξ_n is calculated. Parallel to this process, we check after each step if the solution has exceeded the potential barrier $|\beta_n| > r_-$. If this case occurs, the simulation created a tunneling event and is therefore stopped. The tunneling time is given by $\tau = n\Delta t$, where n is the final step which satisfied the tunneling condition. Accordingly, this computation is given by a while-loop with the condition $|\beta_n| < r_-$ which iteratively solves the recursive series.

This process is visualized in Fig. 4.2 for two differently strong thermal fluctuations. Figure 4.2a represents strong thermal fluctuations. Here, we can see that the realization of β_n propagates towards the top left unstable fixed r_-, but the trajectory does not escape via this fixed point. This changes for smaller fluctuations, which is presented in Fig. 4.2b. In this case, the realization of β_n is triangle-shaped and escapes approximately via the bottom left fixed point r_-. This triangular shape indicates that it is energetically favorable for the solution to propagate in the direction of the unstable fixed points. This exceeds the expectations which we proposed in Sec. 4.3, where we assumed that solution escapes via one of the unstable fixed points because these are the shortest paths between the center $r = 0$ and the colored regions. Therefore, to ensure that the escape over the potential barrier occurs mainly via unstable fixed points, we investigate the tunneling process for small thermal fluctuations and, hence, for large tunneling times, *i. e.* $E_-/k_BT \gg 1$.

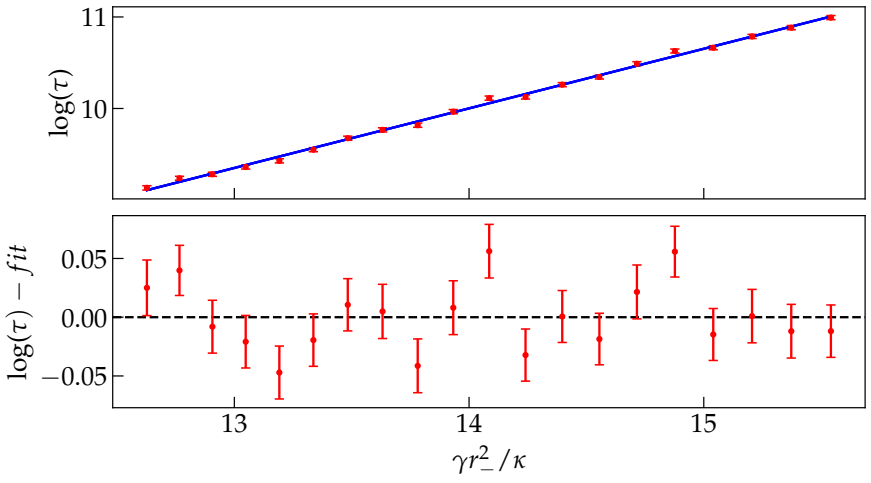

Figure 4.3: The top plot presents the linear regression for the logarithmic tunneling time $\log(\tau)$ versus $\gamma r_-^2/\kappa$ for the parameters $\epsilon = 10\alpha$, $\gamma = 10\alpha$, $\Delta = 0$ and thermal fluctuations in the range $\kappa \in [6.5, 8] \times 10^{-2}\gamma$. The bottom plot shows the residual of the regression.

Now, we continue with the determination of the tunneling time. Since the process we discussed to determine τ is statistical, it has to be repeated multiple times to receive a meaningful result. Therefore, we repeat the process $N = 1000$ times and calculate the average tunneling time $\langle\tau\rangle$ and the corresponding error on the average, which yields

$$\tau = \langle\tau\rangle \pm \frac{\sigma_\tau}{\sqrt{N}}. \tag{4.37}$$

The average value is calculated via the arithmetic mean and the error is given by the standard deviation of the data set divided by $\sqrt{N}$ to obtain the uncertainty on the average value.

Furthermore, to check if Eq. (4.35) describes the correct dependency of κ, we determine the average tunneling time for multiple values of κ and investigate the behavior of the resulting function. Since we expect the exponential dependency given by Eq. (4.35), we plot the logarithm of the tunneling time versus $\gamma r_-^2/\kappa$. We expect the resulting data are linearly increasing with a slope of $2/3$. Therefore, we apply a linear regression on the data points such that we obtain the slope and the axis interception with the corresponding errors.

The linear regression is presented in Fig. 4.3. First of all, the goodness of the fit is given by $\chi^2/n_{\text{dof}} \approx 1.77$, which implies that the behavior of the curve can be, as a valid approximation, described by a linear function. In addition, the residual plot does not show any systematics, which supports this statement. Furthermore, the slope of the fit is given by $C = 0.651 \pm 0.006$, which lies in a range of approximately 2.6σ to the expected value of $2/3$. Thus, this result is in agreement with the expectations because it is within a range of 3σ.

However, we cannot confirm the dependency of r_-^2 if only the fluctuations κ are varied. To this end, we repeat this simulation and the corresponding evaluation for ten different values of ϵ, resulting in ten different distances between the origin $r = 0$ and the unstable fixed points r_-.

The results of each simulation are presented in one plot, which is shown in Fig. 4.4. Since the results of the simulations are compatible with each other, the plot also contains the weighted average (red), which is given by

$$C_{\text{WA}} = 0.664 \pm 0.003. \tag{4.38}$$

This result lies within one standard deviation of the analytical result, which implies that the numerical simulations are in agreement with the analytical calculations.

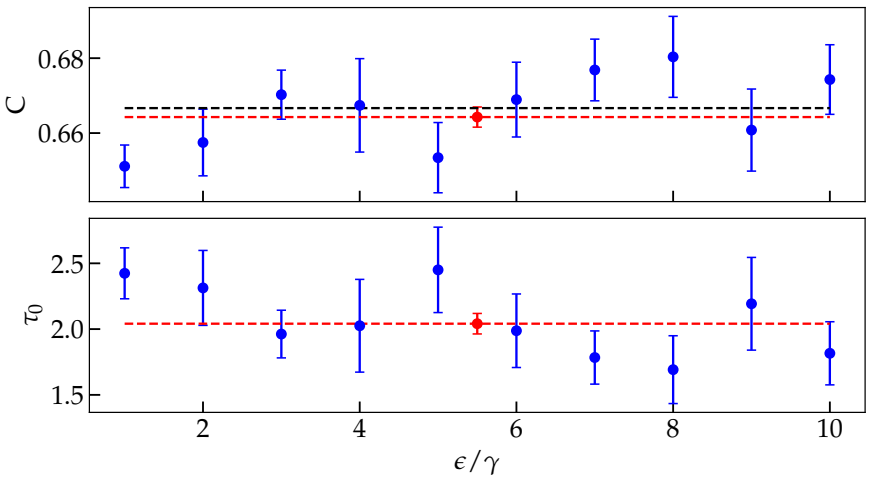

Figure 4.4: Comparison of the parameters for the fit $\tau = \tau_0 e^{C\gamma r_-^2/\kappa}$ for ten different values of ϵ/γ (blue), and the parameters $\alpha = \gamma/10$ such as $\Delta = 0$. The top plot presents the slopes of the linear regressions, which was exemplary presented in Fig. 4.3, and the bottom plot contains the exponential of the axis intersects of the linear regressions. The corresponding error is calculated via Gaussian propagation of error. Both plots contain the weighted average, represented by the red dashed line and the red error bar.

Furthermore, we find that the parameter τ_0 does not change for different values of ϵ/γ, which is an extension to the analytical result, where we only determined the tunneling rate to an exponential accuracy. Thus we can also calculate the weighted average for this case

$$\tau_0 = 2.041 \pm 0.078. \tag{4.39}$$

Additionally, we expect that τ_0 is independent of the stabilizing strength α, since this force has a negligible influence on the region between $r = 0$ and r_-.

5

BEYOND THE ROTATING-FRAME APPROXIMATION

Finally, we revisit the system in the laboratory frame of reference, which is described by Eq. (2.1). In order to execute the rotating-frame approximation, we chose the ansatz $x = \Re[\beta(t)e^{-i\frac{\Omega}{3}t}]$. We neglected all terms in the limits $\dot{\beta}/\beta,\ \Gamma,\ \Delta \ll \omega_0,\ \ddot{\beta}/\beta \ll \omega_0^2$, and furthermore, all fast oscillating terms. In order to check under which circumstances the approximations were reasonable, we first define the Poincaré map[1]

$$P:\ x(t) \to x\left(t + \frac{6\pi}{\Omega}\right). \tag{5.1}$$

Due to the ansatz for $x(t)$, we find the following behavior of the Poincaré map $x(t + 6\pi/\Omega) = \Re[\beta(t + 6\pi/\Omega)e^{-i\Omega/3t}]$, which implies that the time steps $\Delta t = 6\pi/\Omega$ correspond to a full rotation in the rotating-frame. Thus, the Poincaré map reveals the behavior of $\Re[\beta]$, in a discrete way. Now, if we calculate the derivative of x, in order to create a phase-space diagram, we find $\dot{x} = \Re(\dot{\beta}e^{-i\Omega/3t}) + \Omega/3$ $\times\, \Im(\beta e^{-i\Omega/3t})$. Since we expect β to change very slow in comparison to the oscillation $e^{-i\Omega/3t}$, the first term can be neglected. Thus, when the Poincaré map is applied on $\dot{x}$, we obtain the behavior of $\Im[\beta]$ analogous to the real part. Therefore, we expect to obtain a similar plot as the stability map in Fig. 3.2a, if the approximations are correct.

The resulting Poincaré maps of the phase space with a normalized y-axis are shown in Fig. 5.1. In Fig. 5.1a, we find that the Poincaré stability map leads to an almost identical result as the stability map in Fig. 3.2a. This implies that the rotating-frame approximation is valid for large enough resonance frequencies. However, the restriction $\dot{\beta}/\beta \ll \omega_0$ can only be satisfied if the oscillation of β changes significantly slower over time than $e^{-i\omega_0 t}$. As already discussed in Sec. 3.3, the limit of the oscillation frequency ω is given by $\omega = \sqrt{3}\epsilon^2/\alpha \approx 17\epsilon$, for $\epsilon = 10\alpha$. Due to the increase of ω for greater distances from the outer fixed points, the rotating-frame approximation only holds in a limited region around the origin, as long as $\omega_0 \gg \omega$ is satisfied. In Fig. 5.1b we can see the effects of an insufficiently small resonance frequency. In this case, the region near the origin has a similar form as in Fig. 5.1a but it is deformed and asymmetric. For greater distances, this effect increases rapidly. The trajectories which lead to the fixed

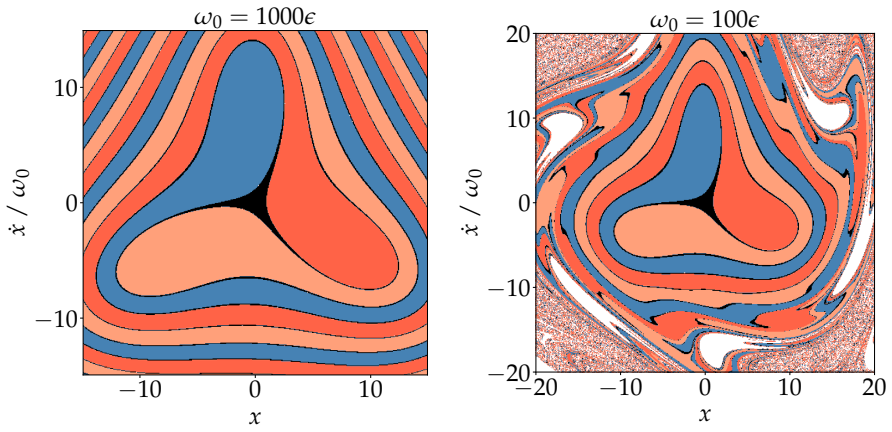

(a) (b)

Figure 5.1: Poincaré stability maps for the parameters $\epsilon = 10\alpha$, $\gamma = 10\alpha$, $\Delta = 0$, and two different resonance frequencies $\omega_0 = 1000\epsilon$ (a), $\omega_0 = 100\epsilon$ (b). Each position on this map represents an initial condition and the color indicates the fixed point the Poincaré map of the solution for $x(t)$ converges to. To this end, the fixed points we discussed earlier were used, since we expected an analogous behavior to the rotating-frame. The white regions in Fig. (b) describe solutions that could not have been identified with the fixed points we calculated.

points are wavy and there are regions (white), which do not converge to any of the known fixed points. These regions are considered to be no fixed points because the endpoint of the Poincare map depends on the simulation time. This means that the solution of $x(t)$ has stable oscillating trajectories, which cannot be analyzed with the Poincaré map in Eq. (5.1) because the dominating oscillation frequency is greater than $\Omega/3$. Further, beyond the white regions, Fig. 5.1b reveals chaotic areas where all five colors seem to be represented randomly. Here, a very small change of initial conditions results in a different endpoint.

6

CONCLUSION

This thesis analyzed period tripling in a Duffing-oscillator which is parametrically driven at thrice its resonance frequency. In Ch. 2 we discussed numerical solutions and the frequency spectra, which led to a first approach for the investigation. We found a threefold symmetry in the form of an invariance under the time translations $t \to t + 2\pi n/\Omega$, where $n \in \{0, 1, 2\}$, which is the origin of period tripling. Both findings led to the ansatz of the rotating-frame approximation with a complex amplitude, which resulted in a convenient description of period tripling.

This ansatz led to a differential equation for the amplitude, which we studied in Ch. 3. There, we found that period tripling is only obtained if the driving strength exceeds the limit $\epsilon_{\min} = \sqrt{2\gamma\alpha}$ in dependence on the stabilizing strength α and the dissipation γ, which is consistent with our physical expectations. Additionally, we found a potential barrier between the stable fixed points $r = 0$ and the outer fixed points r_+ in the form of the unstable fixed points r_-.

In Ch. 4, we included thermal fluctuations in the form of white noise and analyzed the limit of small fluctuations, *i. e.* $E_s/k_BT \ll 1$. We found that these fluctuations can induce period tripling due to tunneling from the regime of a vanishing oscillation amplitude $r = 0$ to the outer fixed points r_+. We analytically determined the average tunneling time to an exponential accuracy $\tau \propto \exp(E_-/3k_BT)$, which we validated afterwards by numerical simulations. Moreover, we showed that, for small fluctuations, the escape over the potential threshold happens mainly over the unstable fixed points r_-.

At the end of our examinations, in Ch. 5 we revisited the system beyond the rotating-frame approximation. We showed that this approximation is only valid if the resonance frequency ω_0 is much larger than all parameters and especially than the rate of change of β. If this criterion is not satisfied, the system becomes asymmetric and obtains additional oscillations which cannot be described by an ansatz that only considers one oscillation frequency. Thus, we were able to describe the system correctly via the rotating-frame approximation.

However, the Duffing-oscillator is more complex than we discussed within the scope of this thesis.

7

BIBLIOGRAPHY

[1] Private discussion with M. Sc. L. Otten.

[2] Lisa Arndt and Fabian Hassler. *Period tripling due to parametric down-conversion in circuit QED*. Physical Review Letters, 128(18): 187701, (2022).

[3] Ismail A. Buliyaminu. *On the classical derivation of electrodynamic equations from the stationary action*. International Journal of Innovative Science and Research Technology, 4: pages 869–873, (2019).

[4] Eugene I Butikov. Parametric excitation of a linear oscillator. European Journal of Physics, 25(4):535–554, may 2004.

[5] M. Chaichian and A. Demichev. *Path Integral in Physics: Volume 1: Stochastic Processes and Quantum Mechanics*. Institute of Physics Publishing Bristol and Philadelphia, (2011).

[6] Daniel T Gillespie. *Fluctuation and dissipation in Brownian motion*. American Journal of Physics, 61(12): pages 1077–1083, (1993).

[7] A. Kamenev. *Many-Body Theory of Non-Equilibrium Systems*. pages 33–35.

[8] Dani Martı. *A short tutorial on the path integral formalism for stochastic differential equations*. pages 5–7

[9] Wolfgang Nolting. Grundkurs Theoretische Physik 2: Analytische Mechanik. Springer-Verlag, pages 112–115, (2010).

[10] Wolfgang Nolting. *Theoretical Physics 8: Statistical Physics*. Springer Nature, (2018).

[11] L. Otten. *Dual shapiro steps of a phase-slip junction in the presence of a parasitic capacitance*. M. Sc. thesis, RWTH Aachen University

page 17, (2018).

[12] Dennis V Perepelitsa. *Johnson noise and shot noise*. Dept. of Physics, MIT, (2006).

[13] Robert M. Wald. *General Relativity*. University of Chicago Press, (1984).